THE JOURNAL OF PHYSICAL CHEMISTRY C
A JOURNAL OF THE AMERICAN CHEMICAL SOCIETY

pubs.acs.org/JPCC

Article

# Employing Optical Emission Spectroscopy to Elucidate the Impact of Titanium Dioxide in Plasma-Assisted Catalysis

Tara L. Van Surksum and Ellen R. Fisher*

**Cite This:** *J. Phys. Chem. C* 2021, 125, 3924−3939

Read Online

ACCESS | Metrics & More | Article Recommendations | SI Supporting Information

**ABSTRACT:** The roles of gas phase, gas−surface interface, and material properties of the catalyst must be understood to fully realize future applications of plasma-assisted catalysis (PAC) for pollution remediation. This requires understanding of fundamental processes contributing to plasma−catalyst synergy, including determination of molecular temperatures. Optical emission spectroscopy (OES) was employed for gas-phase processes in $H_2$ and $CH_4$ inductively coupled plasmas in the presence of catalytic $TiO_2$. $TiO_2$ introduction has a minimal effect on the rotational temperature of $H_2$ [$T_R(H_2)$] in 100% $H_2$ plasmas but reduces $T_R(H_2)$ by ≤300 K in 100% $CH_4$ plasmas. Time-resolved OES studies echo energy partitioning results and reveal further kinetic details on $H_2$ formation and the impact of catalysts on gas-phase processes. Comprehensive analysis of the catalyst before and after plasma exposure reveals $H_2$ plasmas act as etching systems whereas competing etching and deposition processes occur under some conditions in $CH_4$ plasmas.

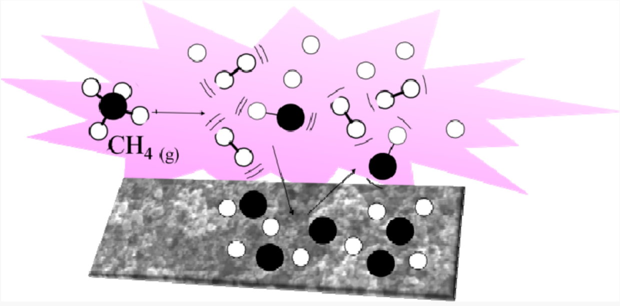

## 1. INTRODUCTION

Plasma-assisted catalysis (PAC) has recently gained attention in the plasma community because of its enormous potential to enhance feed gas conversion.[1−3] Generally, PAC describes the coupling of a plasma with a catalyst for enhanced processing of the input gas stream either to convert the feed gas mixture to another gas mixture or to grow a material from the precursor gas. For example, in plasma-enhanced chemical vapor deposition (PECVD) systems used for fabrication of carbon nanostructures, a hydrocarbon plasma is typically brought into contact with a catalyst (usually Ni, Fe, or Co).[4] PAC, however, is more traditionally used to describe waste gas stream processing such as for the abatement of volatile organic compounds[5−7] or hydrocarbon reforming for the production of value-added chemicals such as syngas or methanol.[8−10] Significant efforts have been devoted to the design and development of catalysts in conventional thermal reforming processes;[11−13] yet, the knowledge of selecting appropriate catalysts for plasma reforming processes is still limited. Jurkovic et al. examined methane partial oxidation processes in plasma utilizing several types of zeolite- and metal-based catalysts.[14] Their results highlight the effects of catalyst choice on conversion, product yield and selectivity, and coking for the overall process. Zeng et al. examined the addition of promoters (e.g., K, Mg, and Ce) to a $Ni/Al_2O_3$ catalyst for enhanced plasma−catalytic biogas reforming.[15] Although the conversion of $CH_4$ and the yield of $H_2$ were improved with the addition of promoters, increased carbon deposition was also observed.

These studies demonstrate that the plasma/catalyst combination generates synergistic effects that can enhance conversion, product selectivity, and energy efficiency. Importantly, it has been suggested that the observed plasma/catalyst synergy results from a combination of the change in discharge behavior induced by the catalyst and change in the catalyst activity assisted by the plasma.[16] Brune et al. investigated the change in filamentary behavior in a packed bed dielectric barrier discharge (DBD) during dry reforming of methane, correlating their observations with conversion efficiencies and material analyses.[17] Differences in conversion efficiencies between each metal-based catalyst (Co, Cu, and Ni) were explained by through differences in electrical behavior of the discharge and material surface properties. Chawdhury et al. found that an Fe/$\gamma$-$Al_2O_3$ plasma/catalyst combination nearly doubled methane conversion and methanol yield compared to a plasma without a catalyst, whereas a Cu/$\gamma$-$Al_2O_3$ catalyst enhanced selectivity of $C_n$ ($n \geq 2$) oxygenates.[18] As catalyst/discharge coupling significantly affected $CH_4$ conversion, plasma emission was explored to gain insight into gas-phase reactions occurring at the catalyst surface. Decreased emission intensity for several species in the presence of the catalyst indicates some reactive plasma species may adsorb on the catalyst surface. The authors suggest that

**Received:** November 29, 2020
**Revised:** February 2, 2021
**Published:** February 10, 2021

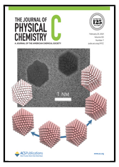

https://dx.doi.org/10.1021/acs.jpcc.0c10698

**Table 1. Internal Temperature Values and Trends from 100% $H_2$ and 100% $CH_4$ Plasmas, sans Catalyst (Reported Previously)[25,26]**

| | 100% $H_2$ | 100% $CH_4$ | | |
|---|---|---|---|---|
| | $T_R(H_2)$ | $T_R(H_2)$ | $T_R(CH)$ | $T_V(CH)$ |
| internal temp value range (K) | ∼500−550 | ∼500−700 | ∼1750−2350 | ∼2280−3440 |
| press. increase (100 → 200 mTorr) | no trend | increases | decreases | decreases |
| power increase (25 → 125 W) | no trend | decreases | trend dependent on system pressure | trend dependent on system pressure |

enhanced plasma−catalyst performance arises from a combination of plasma−surface and plasma gas-phase reactions plus changes in discharge properties (e.g., enhanced electric field). Direct adsorption of gas-phase $CH_x$ radicals is central to methanol formation. Thus, understanding the underlying mechanisms associated with hydrocarbon reforming processes is crucial to its development.

To improve the utility of PAC, it is crucial to understand and optimize the underlying physicochemical mechanisms for their desired applications. Although many studies have focused on parametric optimization for increasing gas conversion efficiency,[19−22] relationships between plasma parameters and performance are ultimately poorly understood, making it tedious and time-consuming to try to reproduce similar results in different reactor setups. Few studies have addressed fundamental aspects of PAC systems. Specifically, the need for fundamental insight into this field requires an understanding of plasma generation and general operating conditions, catalyst selection (including consideration of both chemical and physical properties), and the interactions between the plasma and catalyst. Importantly, an understanding of how the plasma affects the catalyst properties and vice versa must also be construed to address current challenges with implementing PAC technologies. As such, fundamental investigations that probe the molecular-level processes in PAC are central to improving PAC processes.

Knowledge of the roles of gas-phase radicals and radical−surface interactions is key to understanding overall plasma chemistry. To further illuminate the effect of the catalyst on the plasma environment, it is vital to investigate the gas-phase chemistry of the plasma both with and without a catalyst. Specifically, an understanding of how energy is partitioned into vibrational, rotational, and translational modes provides insight into formation mechanisms, decomposition pathways, and overall plasma chemistry. Figures of merit such as rotational and vibrational temperatures ($T_R$ and $T_V$, respectively) describe the energetics of species within the plasma system. One study that examined the impact of a catalyst on internal plasma temperatures measured $T_R$ and $T_V$ of CH $A^2\Delta \rightarrow X^2\Pi$ in a packed bed DBD using optical emission spectroscopy (OES).[23] Nozaki et al. found that although $T_R$(CH) was dependent on the catalyst bed temperature, $T_R$(CH) remained unchanged upon addition of the catalyst to the reactor.[23] The explanation for this observation lies in the assumption that the rotational equilibrium of CH $A^2\Delta$ is reached within its radiative lifetime and that the R branches display a similar intensity distribution with or without the catalyst. In contrast, $T_V$(CH) increased significantly with bed temperature only when the Ni catalyst was present. Specifically, the relative intensity of the $\nu(2,2)$ vibrational band remained independent of bed temperature, but decreases in the $\nu(0,0)$ and $\nu(1,1)$ vibrational bands were observed as the bed temperature increased only with the catalyst present. Consequently, the decreased contributions of the $\nu(0,0)$ and $\nu(1,1)$ vibrational bands to the overall spectral structure result in the observed increase in vibrational temperature in the presence of the catalyst. As the electric and optical properties (e.g., reduced field strength, average electron density, and rotational temperature) were not affected by the presence of the Ni catalyst,[23,24] the authors hypothesize that the CH $A^2\Delta$ $\nu(0,0)$ and $\nu(1,1)$ states selectively react on the Ni surface.

We have previously investigated energy partitioning trends of CH $A^2\Delta \rightarrow X^2\Pi$ and $H_2$ $d^3\Pi_u \rightarrow a^3\Sigma_g^+$ in $CH_4$-based low-pressure, inductively coupled plasmas as functions of plasma parameters.[25,26] An overview of the internal temperature values and parameter trends determined from 100% $H_2$ and 100% $CH_4$ plasmas and sans catalyst is displayed in Table 1. Notably, $T_V$(CH) was higher than $T_R$(CH) regardless of gas mixture, pressure, or power, and both $T_V$(CH) and $T_R$(CH) decreased with increasing pressure, suggesting collisional quenching. $T_R$(CH) values were also nominally much higher than $T_R(H_2)$ values in a 100% $CH_4$ plasma system (Table 1).

Moreover, studies using a 100% $H_2$ plasma reveal relatively low $T_R(H_2)$ values (∼500−550 K) with virtually no trends with respect to system pressure and power.[26] These disparate values and trends may be attributed to a combination of the differences in species densities, radiative lifetimes, and their excitation pathways. In this work, we expand on these fundamental studies by introducing a $TiO_2$ catalyst to $H_2$ and $CH_4$ plasmas. We examine the impact of the plasma on the catalyst by exploiting chemical and morphological characterization techniques to assess the material prior to and post plasma exposure. Additionally, we investigate the impact of the catalyst on gas-phase chemistry via OES, which allows us to nonintrusively probe the energetic and kinetic characteristics of the system. $T_R$ and $T_V$ are measured for three excited-state species (CH, $H_2$, and OH) and are discussed in comparison to values obtained without a catalyst.

## 2. EXPERIMENTAL SECTION

**2.1. Plasma Reactor.** Inductively coupled plasmas were generated in a glass tubular reactor by coupling of radiofrequency (rf) power through a Ni-plated Cu induction coil (Figure 1). Substrates were placed on a glass slide in the center of the coil region, and the reactor was evacuated to base pressure (∼15 mTorr) with a 400 L/min rotary vane pump. The system pressure ($p$) was monitored with a Baratron capacitance monometer and ranged from 100 to 200 mTorr for the experiments described herein. $CH_4$ (Air Products, >99.97% purity), $H_2$ (Airgas, 99.9%), and Ar (Airgas, >99.999% purity) were used as precursor gases with gas flow maintained by mass flow controllers (MKS). The applied rf power ($P$) ranged from 25 to 125 W and was controlled with an Advanced Energy RFX-600 rf power supply via a matching network at 13.56 MHz. A replaceable quartz window on the inlet half of the reactor was used to monitor relative species densities directly above the substrate. All other OES studies described herein utilized a second quartz window centrally affixed to the

https://dx.doi.org/10.1021/acs.jpcc.0c10698
J. Phys. Chem. C 2021, 125, 3924−3939

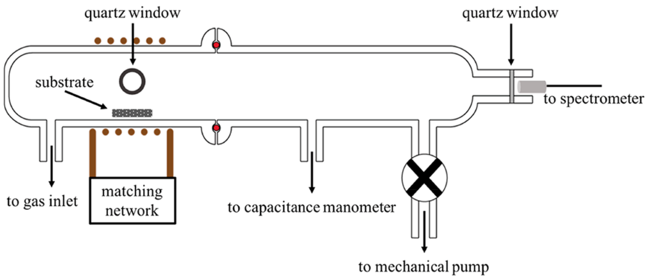

**Figure 1.** Schematic for glass barrel style ICP reactor detailing substrate placement in coil region and quartz window positions for collection of emission spectra. OES spectra were obtained both coaxially and in the coil region.

downstream end of the reactor, allowing for coaxial collection of plasma emission along the length of the reactor.

**2.2. Gas-Phase Analyses.** Steady-state emission experiments employed an Avantes AvaSpec-3648-USB2 multichannel spectrometer with an integration time of 50 ms and 100−150 averages. This spectrometer comprises four channels each linked to a 3648-pixel charge-coupled detector providing a detectable wavelength range of 187−1016 nm with a 0.1 nm resolution. Energy partitioning trends for $H_2$ $d^3\Pi_u \rightarrow a^3\Sigma_g^+$ and CH $A^2\Delta \rightarrow X^2\Pi$ are reported as functions of plasma applied rf power and pressure. Figure S1 shows representative emission spectra for these two transitions and the corresponding fits for determination of $T_R$ and $T_V$. Under some plasma parameters, OH $A^2\Sigma^+ \rightarrow X^2\Pi$ emission was observed, and $T_R$(OH) and $T_V$(OH) were subsequently calculated. A Boltzmann plot was used to calculate $T_R(H_2)$, described in detail previously.[26] For these calculations, $\ln(I\lambda^4/S)$ is plotted as a function of the upper state rotational energy ($E$), where $I$ and $\lambda$ are the intensity (au) and wavelength (nm) of a specific emission line, respectively, and $S$ is the Hönl−London factor. A representative Boltzmann plot for calculating $T_R(H_2)$ is shown as an inset in Figure S1a. $T_R$(CH,OH) and $T_V$(CH,OH) were determined with LIFBASE.[27] A thermalized distribution was assumed for computing $T_R$, and a representative best fit of the vibrational state populations was determined by manual manipulation of the vibrational histogram. $T_V$ values were further calculated by the summation of the vibrational populations weighted by Boltzmann's constant ($k_B$). For all $T_R$ and $T_V$ values reported in this work, the error was determined from the standard deviation of $n \geq 3$ trials.

For time-resolved optical emission spectroscopy (TR-OES) data collection, an AvaSpec-ULS4096CL-EVO spectrometer (10 μm slit; 0.5 nm spectral resolution) was employed for enhanced temporal resolution (1.67 μs integration time; 1 average). Data collection started before plasma ignition and lasted for ∼4 s after ignition. The emission intensity for $H_2$ (601.8 nm) was monitored as a function of time in $H_2$ and $CH_4$ plasmas.

**2.3. Material Preparation and Characterization.** $TiO_2$ substrates were prepared from a methanol suspension of commercial $TiO_2$ AEROXIDE P25 nanopowder (Acros Organics, 21 nm primary particle size) drop cast onto ∼3 cm × 3 cm glass slides (VWR), p-type ⟨100⟩ silicon wafers (Wacker-Chemitronic GMBH), or pressed KBr pellets (Sigma-Aldrich, FTIR grade). One substrate was placed in the center of the coil region of the reactor for OES experiments (Figure 1). KBr pellets with $TiO_2$ were used for Fourier transform infrared spectroscopy (FTIR) (Nicolet Magna 760). The spectrometer was purged with $N_2$ gas for several hours before spectra were collected (4 $cm^{-1}$ resolution; 256 averaged scans). Atmospheric and baseline corrections were applied to all spectra to suppress signals arising from water vapor or $CO_2$. Silicon wafer substrates were further characterized by using scanning electron microscopy (SEM) (JEOL JSM-6500F with a field emission source; 15.0 kV accelerating voltage; ∼10 mm working distance). Glass slide substrates were used for all other characterization methods. X-ray photoelectron spectroscopy (XPS) [PHI-5800 with a monochromatic Al Kα X-ray source (1486.6 eV photons)] was performed before and after plasma exposure. CasaXPS v2.3 software was used to evaluate all high-resolution XPS data with peak FWHM constrained to ≤2.0 eV. High-resolution $C_{1s}$ spectra were charge corrected by setting the C−C/C−H component to 284.8 eV for all samples. Raman spectroscopy data were collected with an Olympus IX-73 optical microscope with an OndaxTHz-Raman laser source (5 mW, 532 nm laser, 1.2 μm spot size). Raman signals were collected in a backscattering geometry, passed through a Horiba iHR-550 imaging spectrometer, and detected on a Synapse back-illuminated deep depletion charge-coupled device. Individual spectra were acquired for 30−60 s across a 1 mm × 1 mm sample area.

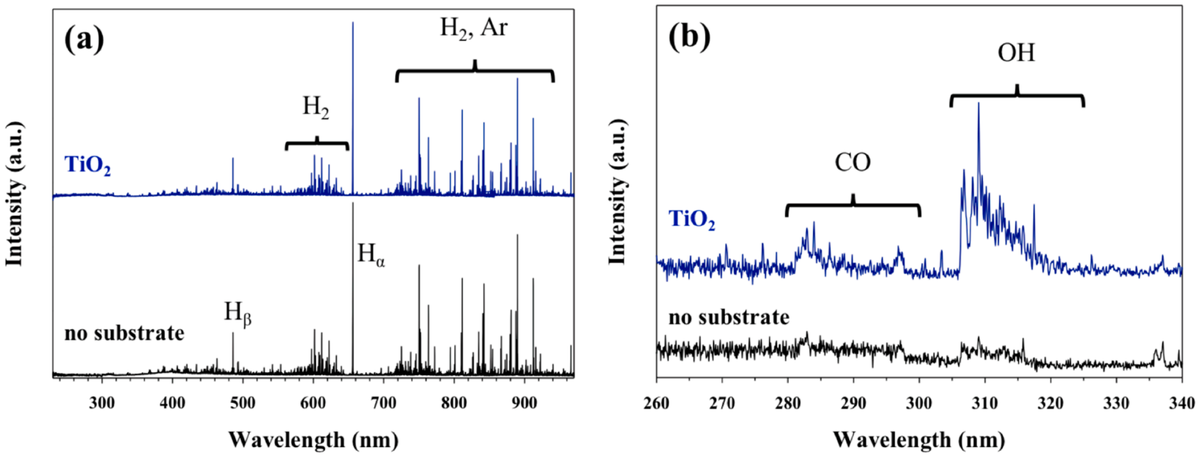

**Figure 2.** Raw OES spectra of $H_2$ plasma ($p$ = 100 mTorr, $P$ = 100 W, and $t$ = 30 s) collected coaxially without a substrate and with a $TiO_2$ substrate: (a) full spectral range and (b) expanded view of the 260−340 nm range.

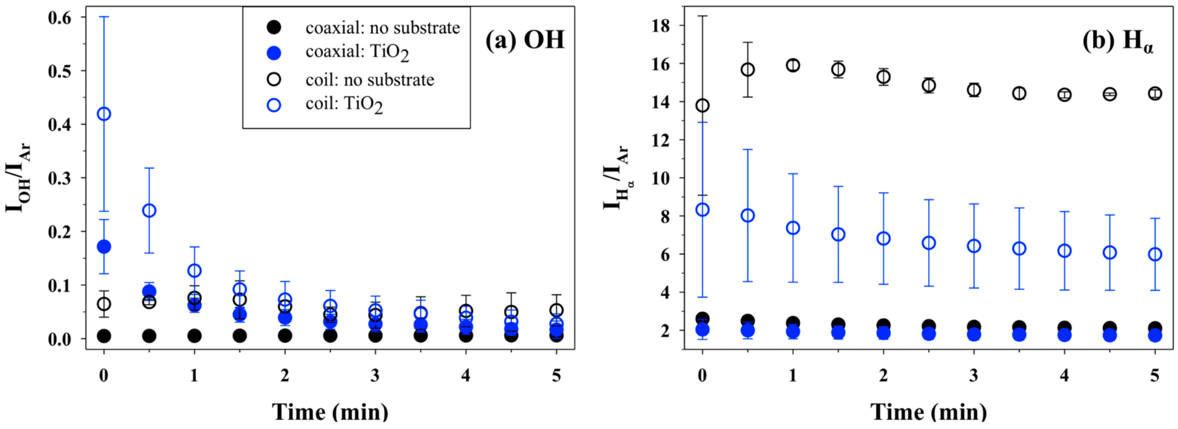

**Figure 3.** Relative density from OES spectra collected coaxially and in the coil region of the reactor as a function of time in an $H_2$ plasma ($p$ = 100 mTorr and $P$ = 125 W) with and without a $TiO_2$ substrate for (a) OH and (b) $H_\alpha$.

## 3. RESULTS

A major focus of this work is to investigate fundamental plasma−catalyst interactions in environmentally relevant systems. Our multipronged approach toward unravelling complex PAC environments involves an investigation of both the gas-phase processes and an analysis of the catalyst's chemical and morphological properties. Raw OES spectra of a $H_2$ plasma (10% Ar) show emission arising from atomic and molecular hydrogen species and Ar species (Figure 2a). With a $TiO_2$ substrate present, additional spectral peaks are observed, arising from OH and CO emission (Figure 2b). As these species are not detected above experimental noise in the substrate-free system, OH production likely occurs through removal of oxygen from the $TiO_2$ catalyst, and the small amounts of $CO_{(g)}$ also likely arise via interaction of gas-phase species with adventitious carbon on the catalyst surface.

Further spectral comparison via inert gas actinometry elucidates details about relative densities of excited-state species (denoted here with brackets, e.g., [OH]). For these studies, emissions from OH (309.0 nm), $H_\alpha$ (656.5 nm), $H_2$ (601.8 nm), and Ar (750.4 nm) were monitored. Actinometry studies were performed for several power conditions in $H_2$ plasmas ($p$ = 100 mTorr) both with and without $TiO_2$ for 5 min immediately following plasma ignition. Measurements were made at two locations: in the coil region directly above the substrate (cross-sectional) and downstream (coaxial). Figure 3a shows [OH] as a function of time ($p$ = 100 mTorr and $P$ = 100 W) with and without $TiO_2$ present in the reactor. Notably, [OH] is nearly zero without the substrate; however, when $TiO_2$ is introduced into the plasma, [OH] is initially greater than the no substrate system and then decreases as a function of time. After ∼2 min of plasma on time, the [OH] is within error of the no substrate system and essentially zero for all $P$ studied. Actinometry results from the coil region demonstrate that [OH] may be only slightly elevated compared to the coaxially collected data, suggesting that when OH is formed from plasma−substrate interactions, it likely remains intact as it travels downstream in the reactor.

Actinometric analysis of hydrogen species in the plasma provides insight into the impact of $TiO_2$ on gas-phase properties. [$H_2$] remained relatively constant as a function of time (Figure S2), and both the addition of the catalyst and the measurement location essentially have no effect on [$H_2$]. Yet, the atomic hydrogen density is significantly elevated in the coil region compared to the coaxially collected data (Figure 3b). This is expected given the constant source of $H_2$ gas, which can dissociate to form H in the coil region of the reactor. Moreover, [H] does not change appreciably during the 5 min data collection time. This suggests that $H_2$ decomposes in the coil region and H is not likely to recombine to form $H_2$ there, but it may undergo deexcitation or other recombination processes as it continues downstream, leading to the lower density observed with coaxially collected OES data (Figure 3b). With the $TiO_2$ substrate, [H] measured coaxially (i.e., downstream) is slightly lower than the substrate-free system, albeit within error. In the coil region, however, [H] is significantly lower in the presence of the catalyst, indicating that H atoms are likely interacting with the substrate (e.g., to produce the observed $OH_{(g)}$).

To gain further insight into the plasma−substrate interactions and gas-phase processes, the energetics of plasma species can be evaluated as functions of plasma parameters. $T_R$(OH) and $T_V$(OH) values were determined via spectral simulation with LIFBASE, where all fits had peak correlation (PC) values ≥0.89. OES data collected 30 s after plasma ignition were used for determination of $T_R$(OH) and $T_V$(OH) because the OH emission signal was prominent at this time point. Unfortunately, raw OH data could not be analyzed at low $P$ ($P$ = 25−50 W) or high $p$ ($p$ = 200 mTorr) because of limited signal intensity under these conditions. Figure 4 shows a representative fit of the OH $A^2\Sigma^+ \rightarrow X^2\Pi$ transition ($p$ = 100 mTorr, $P$ = 100 W), giving rise to $T_R$(OH) = 2550 K and $T_V$(OH) = 4600 K and with a PC value of 0.96. Although PC values are fairly high for each individual spectrum, indicating reasonable agreement between the experimental data and corresponding simulation, standard deviation weighs in as high as 16% in some cases, as listed in Table 2. Although challenging to illicit trends from these data, we can ascertain an order of magnitude for $T_R$(OH) and $T_V$(OH) and can compare these values to $T_R(H_2)$ in the same plasma system and other $T_R$(OH) and $T_V$(OH) values reported in the literature.[28−31]

To better understand these gas-phase trends and the impact of plasma processing on the catalyst, the substrates were analyzed before and after plasma exposure. Figure 5 shows representative FTIR spectra of untreated (UT) and $H_2$ plasma treated ($p$ = 100 mTorr, $P$ = 100 W, and $t$ = 5 min) $TiO_2$ substrates. The adsorption bands at 3400 and 1630 cm$^{-1}$ are assigned to stretching bands for O−H surface hydroxyl groups and H−O−H physically adsorbed water, respectively.[32]

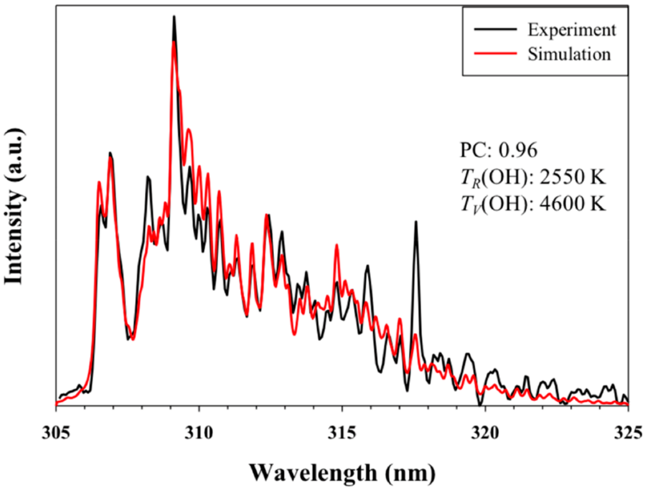

**Figure 4.** Representative emission spectrum collected coaxially for OH $A^2\Sigma^+ \rightarrow X^2\Pi$ in a $H_2$ plasma with a $TiO_2$ substrate ($p$ = 100 mTorr and $P$ = 100 W).

**Table 2. $T_R$(OH) and $T_V$(OH) Values Obtained from a $H_2$ Plasma with a $TiO_2$ Substrate**[a]

| $p$ (mTorr) | $P$ (W) | $T_R$ (K) | $T_V$ (K) |
|---|---|---|---|
| 100 | 75 | 3680 (150) | 4020 (40) |
| | 100 | 2940 (480) | 4430 (250) |
| | 125 | 3370 (290) | 4360 (180) |
| 150 | 75 | 3740 (130) | 4110 (40) |
| | 100 | 3520 (450) | 4310 (220) |
| | 125 | 3680 (230) | 4150 (20) |

[a] Values in parentheses represent the standard deviation calculated from the mean of $n \geq 3$ trials.

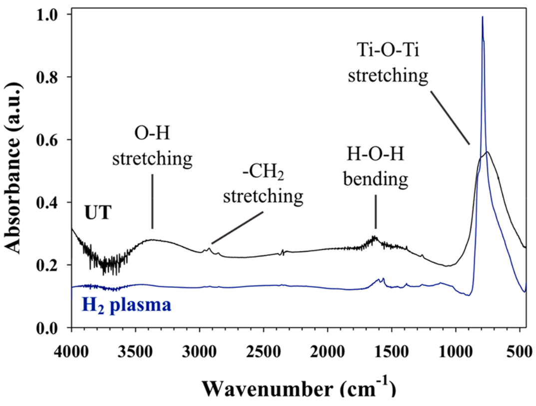

**Figure 5.** FTIR spectra of untreated and $H_2$-plasma-treated ($p$ = 100 mTorr, $P$ = 100 W, and $t$ = 5 min) $TiO_2$ substrates.

Symmetric and asymmetric stretching of $-CH_2$ is observed in the 2830−2990 $cm^{-1}$ region for the UT material.[33] The large absorption band below 1000 $cm^{-1}$ is assigned to Ti−O−Ti stretching vibration of the interconnected octahedral $[TiO_6]$.[32] Some differences worth noting appear when comparing the two spectra. First, the disappearance of the $-CH_2$ peaks and the significant reduction of the O−H stretching band after plasma exposure suggest removal of impurities or cleaning of the material surface by the plasma. Moreover, narrowing of the Ti−O−Ti stretching absorption band post plasma exposure suggests the creation of a more uniform lattice environment and removal of excess impurities.

**Table 3. XPS Atomic Composition Data for a $TiO_2$ Substrate Exposed to a 100% $H_2$ Plasma ($p$ = 100 mTorr)**[a]

| plasma exposure time (min) | $P$ (W) | C [%] | O [%] | Ti [%] |
|---|---|---|---|---|
| | | 10.9 (2.3) | 63.6 (1.4) | 25.5 (1.2) |
| 1 | 125 | 5.6 (0.4) | 68.7 (0.9) | 25.7 (0.6) |
| 5 | 25 | 9.6 (1.9) | 65.0 (1.4) | 25.3 (0.6) |
| | 75 | 5.2 (0.5) | 70.3 (0.9) | 24.5 (0.9) |
| | 100 | 4.8 (0.9) | 72.0 (1.1) | 23.2 (0.8) |
| | 125 | 3.4 (0.6) | 75.9 (3.5) | 20.7 (2.9) |
| 10 | 125 | 3.2 (0.5) | 76.2 (1.5) | 20.6 (1.5) |

[a] Errors are the standard deviation of the mean of three measurements on $n \geq 2$ samples.

We employed XPS to further investigate the chemical composition of the surface of our catalysts before and after $H_2$ plasma exposure. Survey scans conducted on all substrates showed the presence of titanium, oxygen, and carbon prompting the collection of high-resolution data for the $Ti_{2p}$, $O_{1s}$, and $C_{1s}$ binding environments for each spot. Elemental compositions, listed in Table 3, show a decrease in the amount of carbon after $H_2$ plasma exposure. The amount of titanium decreases slightly at high $P$ and longer plasma exposure times ($P$ = 100 W, 125 W, $t$ = 5 min and $P$ = 125 W, $t$ = 10 min). Additionally, an increase in %O is noted after $H_2$ exposure at all conditions except for $P$ = 25 W and $t$ = 5 min. This increase likely arises from the creation of surface oxygen vacancies (verified with high-resolution $O_{1s}$ data, Figure 6), which can allow for increased interactions with atmospheric oxygen. We have previously noted a similar increase in %O with treatment time for $SnO_2$ nanoparticles exposed to a 100% $H_2O$ plasma.[34] Representative high-resolution $Ti_{2p}$, $O_{1s}$, and $C_{1s}$ XPS spectra prior to and post $H_2$ plasma exposure ($p$ = 100 mTorr, $P$ = 150 W, and $t$ = 1 min) are shown in Figure 6. High-resolution $Ti_{2p}$ spectra of the UT $TiO_2$ material (Figure 6a) show peaks for $Ti_{2p3/2}$ and $Ti_{2p1/2}$ at binding energies of 458.8 and 464.7 eV, respectively, corresponding to surface titanium in the $Ti^{4+}$ oxidation state.[35,36] In some cases, $Ti^{4+}$ was reduced (i.e., $Ti^{3+}$ or $Ti^{3+}$ and $Ti^{2+}$ binding environments noted in addition to $Ti^{4+}$) after $H_2$ plasma exposure, whereas in other cases, the $Ti_{2p}$ binding environment remained nominally unchanged post $H_2$ plasma exposure (i.e., only $Ti^{4+}$ binding environments present). Reduction of $Ti^{4+}$ was not dependent on plasma parameters and was somewhat inconsistent between spots on a single sample and/or different samples produced under the same plasma conditions. Figure 6d shows an example of a $Ti_{2p}$ high-resolution spectrum of a spot where $Ti^{4+}$ is reduced to $Ti^{3+}$ (457.8 and 463.6 eV) and $Ti^{2+}$ (456.7 and 462.4 eV) oxidation states. The primary contribution to the $O_{1s}$ spectra in the UT $TiO_2$ arises from lattice bound oxygen (or bound to $Ti^{4+}$) (529.2 eV) (Figure 6b), with a smaller peak assigned to oxygen adsorbed to the material surface, such as hydroxyl species (531.5 eV).[35,37] When Ti is reduced, an additional binding environment appears after hydrogen plasma exposure at 530.5 eV, corresponding to oxygen vacancies (e.g., $Ti_2O_3$).[37] Here, an increase of adsorbed surface oxygen post $H_2$ plasma processing (Figure 6e) is also observed, presumably as a result of the plasma creating oxygen vacancies within the $TiO_2$ lattice, which ultimately decreases the relative contribution of bound oxygen or the increase in adsorbed atmospheric oxygen species.[35,38] High-resolution $C_{1s}$ spectra for the UT material

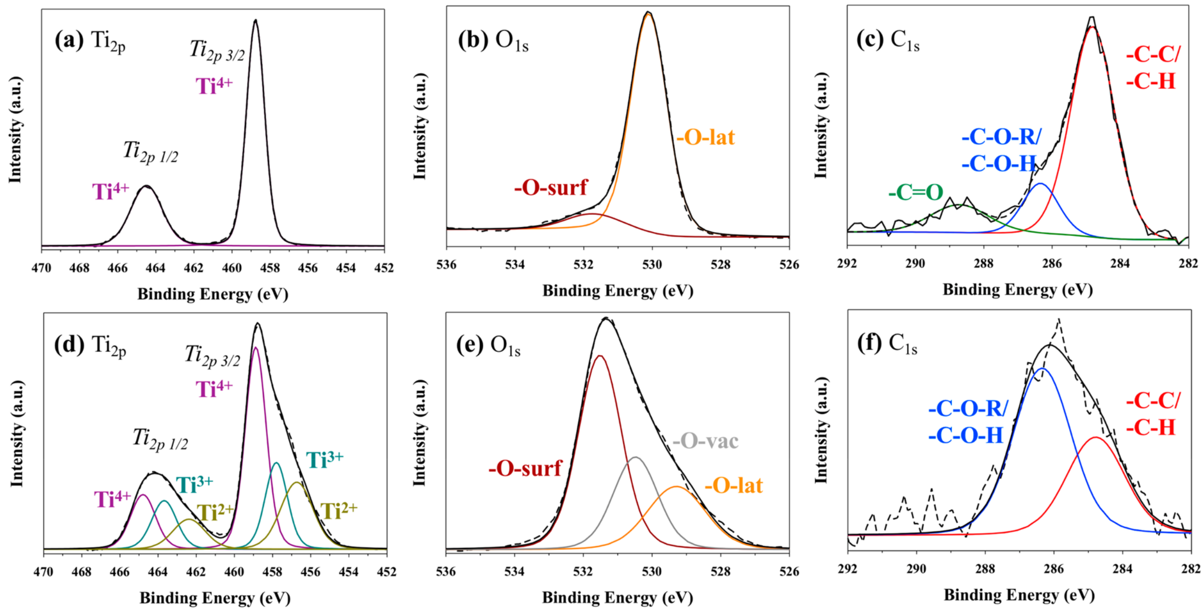

**Figure 6.** High-resolution $Ti_{2p}$ (a, d), $O_{1s}$ (b, e), and $C_{1s}$ (c, f) XPS spectra for untreated (top row) and $H_2$-plasma-treated (bottom row) $TiO_2$ substrates ($p$ = 100 mTorr, $P$ = 125 W, and $t$ = 1 min).

(Figure 6c) show binding environments for −C−C/−C−H (284.8 eV), −C−O−R/−C−O−H (286.3 eV), and −C═O (288.7 eV). The reduction in percent carbon after plasma exposure suggests removal of adventitious carbon (Table 3). Although it is difficult to elucidate specific binding environments with the low C signal, we believe binding environments attributed to −C−C/−C−H (284.8 eV) and −C−O−R/−C−O−H (286.3 eV) are still present in the $H_2$ plasma treated material (Figure 6f).

As $H_2$ plasmas are generally considered etching systems, we also investigated the impact of a clearly depositing system (i.e., 100% $CH_4$ plasmas) on the catalyst. XPS atomic composition data (Table 4) demonstrate a significant increase in %C post $CH_4$ plasma exposure. Moreover, the %C on the surface is highly dependent on plasma parameters. For example, a $TiO_2$ substrate exposed to a 100% $CH_4$ plasma at fairly mild conditions ($p$ = 100 mTorr, $P$ = 25 W, and $t$ = 30 s) results in 51.2% C, whereas 91.7% C is measured under more intense depositing conditions ($p$ = 200 mTorr, $P$ = 125 W, and $t$ = 2 min). Consequently, this drastically changes the O and Ti atomic compositions at the material surface. Interestingly, a slight increase in %Ti is observed from the samples treated for 30 s compared to those exposed to the plasma for 2 min, except at $p$ = 200 mTorr and $P$ = 125 W where no Ti was detected. Generally, the %C increases with $P$ except for the case of $p$ = 100 mTorr and $t$ = 2 min, wherein the atomic compositions for $P$ = 25 and 125 W are within error of each other. Notably, the reported error is also larger for this set of conditions, indicative of the significant variation in atomic surface composition for these samples. The lack of a clear increase in carbon content with $P$ (at $p$ = 100 mTorr and $t$ = 2 min) suggests carbon-containing species are not depositing on the catalyst surface. Although the exact processes contributing to the changes in surface chemistry remain unclear, these results likely indicate competing etching and depositing regimes occurring in this system.

**Table 4. XPS Atomic Composition Data for a $TiO_2$ Substrate Exposed to a 100% $CH_4$ Plasma**[a]

| plasma exposure time | $p$ (mTorr) | $P$ (W) | C [%] | O [%] | Ti [%] |
|---|---|---|---|---|---|
| | | | 10.9 (2.3) | 63.6 (1.4) | 25.5 (1.2) |
| 30 s | 100 | 25 | 51.2 (4.4) | 48.1 (4.3) | <1% |
| | | 125 | 87.9 (2.8) | 9.1 (2.0) | 3.0 (0.8) |
| | 200 | 25 | 84.8 (1.2) | 14.9 (0.8) | <1% |
| | | 125 | 91.3 (2.1) | 7.7 (1.6) | <1% |
| 2 min | 100 | 25 | 77.4 (6.4) | 17.6 (4.4) | 5.1 (2.0) |
| | | 125 | 61.9 (12.8) | 27.8 (8.7) | 10.3 (4.2) |
| | 200 | 25 | 78.4 (2.4) | 18.1 (1.3) | 3.6 (1.3) |
| | | 125 | 91.7 (0.4) | 8.4 (0.4) | |

[a] Errors are the standard deviation of the mean of three measurements on $n \geq 2$ samples.

Further details about the types of films deposited or the possible etching processes occurring in $CH_4$ plasmas can be elucidated from the high-resolution XPS spectra. Figure 7a shows high-resolution $Ti_{2p}$ spectra of an UT $TiO_2$ substrate and $TiO_2$ substrates after a 2 min exposure to a 100% $CH_4$ plasma under several pressure and power conditions. As stated above, binding energies for $Ti_{2p3/2}$ and $Ti_{2p1/2}$ are present at 458.6 and 464.2 eV, respectively, corresponding to surface titanium in the $Ti^{4+}$ oxidation state[35,36] Additionally, contributions from the $Ti^{3+}$ binding environment are noted at 457.9 and 462.5 eV for materials treated at $p$ = 200 mTorr and $P$ = 25 W.[35] High-resolution $O_{1s}$ spectra (Figure 7b) show contributions from lattice bound oxygen at 530.2 eV and adsorbed oxygen species at 532.1 eV for the UT material and after $CH_4$ plasma exposure.[39,40] The $TiO_2$ substrates exposed to a $CH_4$ plasma have an additional peak at 533.3 eV, corresponding to oxygen singly bound to carbon in ethers.[40] Notably, the spectrum acquired under conditions with no detectable Ti in the elemental composition data ($p$ = 200 mTorr and $P$ = 125 W) shows no lattice bound oxygen species, only adsorbed oxygen species and oxygen bound to carbon. High-resolution $C_{1s}$ spectra (Figure 7c) display three specific

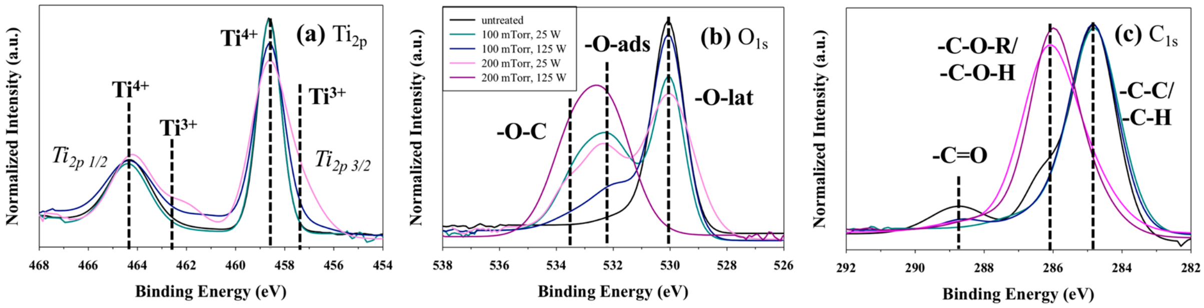

**Figure 7.** High-resolution (a) $C_{1s}$, (b) $O_{1s}$, and (c) $Ti_{2p}$ spectra of $TiO_2$ substrates prior and post $CH_4$ plasma exposure ($t$ = 2 min).

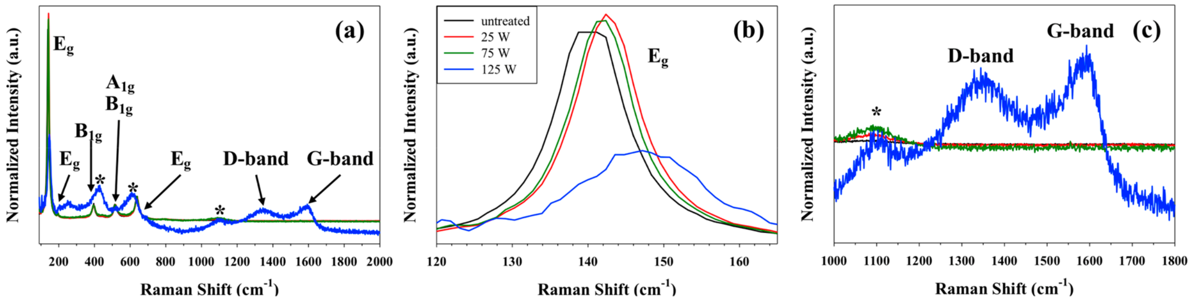

**Figure 8.** (a) Raman spectra of $TiO_2$ substrates [untreated and treated with a 100% $CH_4$ plasma at three applied rf powers ($p$ = 200 mTorr and $t$ = 2 min)]. Expanded views of the (b) $E_g$ peak and the (c) D-band/G-band region. The asterisk (*) represents the signal from the glass slide substrate.

binding environments corresponding to −C−C/−C−H (284.8 eV), −C−O−C/−C−O−H (286.6 eV), and −C=O (288.7 eV).[39] After $CH_4$ plasma exposure, the −C=O contribution decreases significantly, regardless of treatment parameters. Moreover, with $p$ = 200 mTorr, the −C−O−R/−C−O−H contribution increases dramatically relative to the $p$ = 100 mTorr treatment, dominating the spectra for both low- and high-$P$ treatments.

Raman data (Figure 8) also demonstrate the presence of an amorphous hydrocarbon film on the $TiO_2$ after $CH_4$ plasma exposure. Figure 8a shows Raman spectra for UT $TiO_2$ and $TiO_2$ treated with a 100% $CH_4$ plasma ($p$ = 200 mTorr) at different $P$. Anatase $TiO_2$ has six Raman-active modes (3 $E_g$ + 2 $B_{1g}$ + 1 $A_{1g}$).[41,42] The three $E_g$ modes correspond to the high-intensity band at 136 $cm^{-1}$ and the lower-intensity bands at 196 and 638 $cm^{-1}$. Additionally, the doublet band at 515 $cm^{-1}$ corresponds to the $A_{1g}$ and $B_{1g}$ modes, and the band at ∼396 $cm^{-1}$ belongs to the $B_{1g}$ mode.[41,42] Peaks at 429, 608, and 1100 $cm^{-1}$ arise from the glass substrate. Figure 8a demonstrates carbon deposition via the appearance of the D-band and G-band for plasma parameters associated with the most intense deposition conditions in our $CH_4$ plasma systems (high $p$, high $P$). In conjunction with the presence of the D-band and G-band, the more intense deposition parameters also appear to coincide with overall minimized $TiO_2$ bands.

Figure 8b displays an expanded view of the $E_g$ band at ∼135 $cm^{-1}$. The $E_g$ peaks correlate to the symmetric stretching vibration of O−Ti−O in $TiO_2$;[43,44] thus, they are very sensitive to local oxygen coordination surrounding the metal ion. Here, we note a general shift and broadening of the $E_g$ peak at ∼135 $cm^{-1}$ to higher wavenumbers for the plasma treated substrate relative to the untreated $TiO_2$. For example, the higher $P$ plasma treatment ($P$ = 125 W) results in the largest $E_g$ peak shift, 7 $cm^{-1}$, whereas the milder plasma treatments ($P$ = 25 W and $P$ = 50 W) result in less peak shifting, 1−3 $cm^{-1}$, relative to the untreated $TiO_2$. Nevertheless, these data demonstrate that $CH_4$ plasma exposure affects the underlying material beyond deposition of an amorphous hydrocarbon film over the surface of the material.

Figure 8a further demonstrates that carbon deposition throughout the material is observed via the appearance of the D-band and G-band for plasma parameters associated with the most intense deposition conditions (high $p$, high $P$). In conjunction with the presence of the D-band and G-band, these deposition parameters also appear to coincide with overall minimized $TiO_2$ bands. Figure 8c shows an expanded view of the D-band/G-band region for untreated $TiO_2$ and $TiO_2$ post $CH_4$ plasma exposure at $p$ = 200 mTorr and several $P$ conditions. Notably, the D-band and G-band are only present in the spectra acquired from the $P$ = 125 W plasma-treated substrate.

As substrate morphology can impact overall PAC interactions, we used SEM to evaluate material morphology of the UT and plasma-treated $TiO_2$ materials. A representative SEM image of the UT material (Figure 9a) highlights the porous morphological nature of the $TiO_2$ nanoparticle agglomerates. Figures 9b and 9c show representative SEM images of the catalyst after exposure to 100% $H_2$ ($p$ = 100 mTorr, $P$ = 100 W, and $t$ = 5 min) and 100% $CH_4$ ($p$ = 150 mTorr, $P$ = 125 W, and $t$ = 2 min) plasmas, respectively. The morphology characteristic of the UT $TiO_2$ material does not change appreciably after plasma exposure, regardless of $p$ or $P$, for the parameter space reported herein.

Clearly, $H_2$ and $CH_4$ plasmas differentially impact the resulting catalyst chemistry; thus, we compare and contrast the impact of the catalyst on gas-phase chemistry in these two systems. We have previously investigated energy partitioning trends of $T_R(H_2)$ in $H_2$ and $CH_4$ plasmas (no substrate) to elucidate probable mechanisms of $H_2$ formation.[26] Here, we utilized TR-OES to further delve into these fundamental

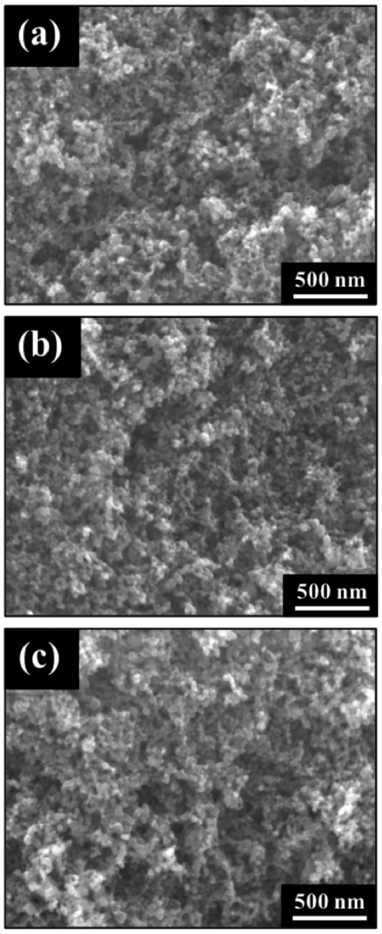

**Figure 9.** Representative SEM images (50000×) of (a) untreated, (b) $H_2$-plasma-treated ($p$ = 100 mTorr, $P$ = 125 W, and $t$ = 5 min), and (c) $CH_4$-plasma-treated ($p$ = 150 mTorr, $P$ = 125 W, and $t$ = 2 min) $TiO_2$ substrates.

processes by studying the first few seconds immediately following plasma ignition in $H_2$ and $CH_4$ plasmas with and without $TiO_2$. Figure 10 shows a comparison of the temporal emission profiles of $H_2$ in the two plasma systems with and without a catalyst. In a 100% $H_2$ plasma, the rise to maximum intensity and subsequent steady-state emission for $H_2$ (Figure 10a) occurs within the first 0.1 s of plasma ignition. Conversely, the rise to a steady state for $H_2$ takes several seconds in a $CH_4$ plasma without a substrate. The overall characteristics of the temporal profiles do not change appreciably upon the addition of a $TiO_2$ substrate to the 100% $H_2$ plasma (Figure 10c). In contrast, the $TiO_2$ dramatically alters the temporal profile of $H_2$ emission in the 100% $CH_4$ plasma (Figure 10d). Here, the temporal profile mirrors the 100% $H_2$ plasma system, with a sharp rise within <0.1 s. These TR-OES data provide essential insight into plasma ignition processes and potential species formation mechanisms; however, evaluation of species energetics is also a key component to understanding fundamental plasma processes during PAC.

$T_R$ values of excited-state $H_2$ are plotted in Figure 11 as a function of $P$ for both $H_2$ and $CH_4$ plasmas with and without $TiO_2$. At $p$ = 100 mTorr (Figure 11a), $T_R(H_2)$ values have a narrow range of ~500−550 K, display minimal power dependence, and remain constant with and without a $TiO_2$ catalyst in the 100% $H_2$ plasma system. Conversely, the $T_R(H_2)$ values in a 100% $CH_4$ plasma without a substrate at $p$ = 100 mTorr (Figure 11a) decrease with increasing $P$, with $T_R(H_2)$ = ~580 and ~500 K at $P$ = 25 and 125 W, respectively. Addition of the catalyst results in a notable decrease in $T_R(H_2)$, with values of ~400−480 K and minimal $P$ dependence at $p$ = 100 mTorr. Similar trends are noted in the higher-pressure system ($p$ = 200 mTorr) (Figure 11b) with $T_R(H_2)$ values elevated somewhat by ~100−200 K for the $CH_4$ plasma system (no substrate). Overall, $T_R(H_2)$ values at $p$ = 200 mTorr for a 100% $H_2$ plasma are similar to those at $p$ = 100 mTorr. Nevertheless, at $P \geq 50$ W, $T_R(H_2)$ values are reduced slightly compared to the no substrate system. Numerical values for all conditions studied with $TiO_2$ are listed in Table 5 and range from ~400−700 K over the entire parameter space. $T_R(H_2)$ values for the no substrate systems (both $H_2$ and $CH_4$) have been previously reported.[26]

To further demonstrate the impact of the catalyst on energy partitioning, $T_R$(CH) is plotted as a function of $P$ at two different pressures in Figure 12a, and $T_R$(CH) values for the entire parameter space are reported in Table 6. At $p$ = 100 mTorr, $T_R$(CH) values are decreased by ~100−200 K with a $TiO_2$ catalyst except at $P$ = 50 W. Interestingly, an increase in system pressure to ≥150 mTorr results in $T_R$(CH) values comparable to those in the no substrate system. Notably, $T_R$(CH) values also decrease concomitantly with an increase in system pressure, a trend we previously reported for 100% $CH_4$ plasmas without a substrate.[25] These results demonstrate the significant impact that catalysts can have on rotational energy partitioning in PAC systems.

Additionally, we determined $T_V$(CH) for the same parameter space (Table 6), where values range from approximately 2000 to 3100 K. Figure 12b shows $T_V$(CH) for a $CH_4$ plasma system without and with a $TiO_2$ substrate at two different pressures. At $p$ = 100 mTorr, $T_V$(CH) is significantly reduced (~300−1200 K) upon addition of the catalyst to the discharge. This trend generally holds true at each pressure ($p$ = 100−200 mTorr). Pressure and power trends for $T_V$(CH) are also worth noting here as $T_V$(CH) values generally decrease with increasing $p$ for $CH_4$ plasmas. The $P$ dependence demonstrates a more complex trend wherein $T_V$(CH) decreases with increasing $P$ at low $p$ ($p$ = 100 mTorr) but increases with $P$ at high $p$ ($p$ = 200 mTorr). This trend has been discussed previously.[25]

## 4. DISCUSSION

As noted in the Introduction, the applicability of PAC is limited by a lack of knowledge of the fundamental processes contributing to plasma−catalyst synergy. Understanding the roles of both the catalyst and plasma as well as the interactions occurring at the plasma−catalyst interface in a PAC system can help the community bypass trial-and-error approaches toward optimizing plasma−catalyst systems and establish a more informed method for optimization toward a desired application. Thus, the goal of this work is both to elucidate the impact of the catalyst on the fundamental properties of the plasma discharge and to understand the effect of plasma exposure on the catalyst's properties. Here, we utilize a nanostructured $TiO_2$ catalyst to report on effects on fundamental plasma processes in low-pressure, inductively coupled $H_2$ and $CH_4$ plasmas. Chemical and morphological properties of the catalyst prior to and post plasma exposure were assessed in addition to the gas-phase studies as a more

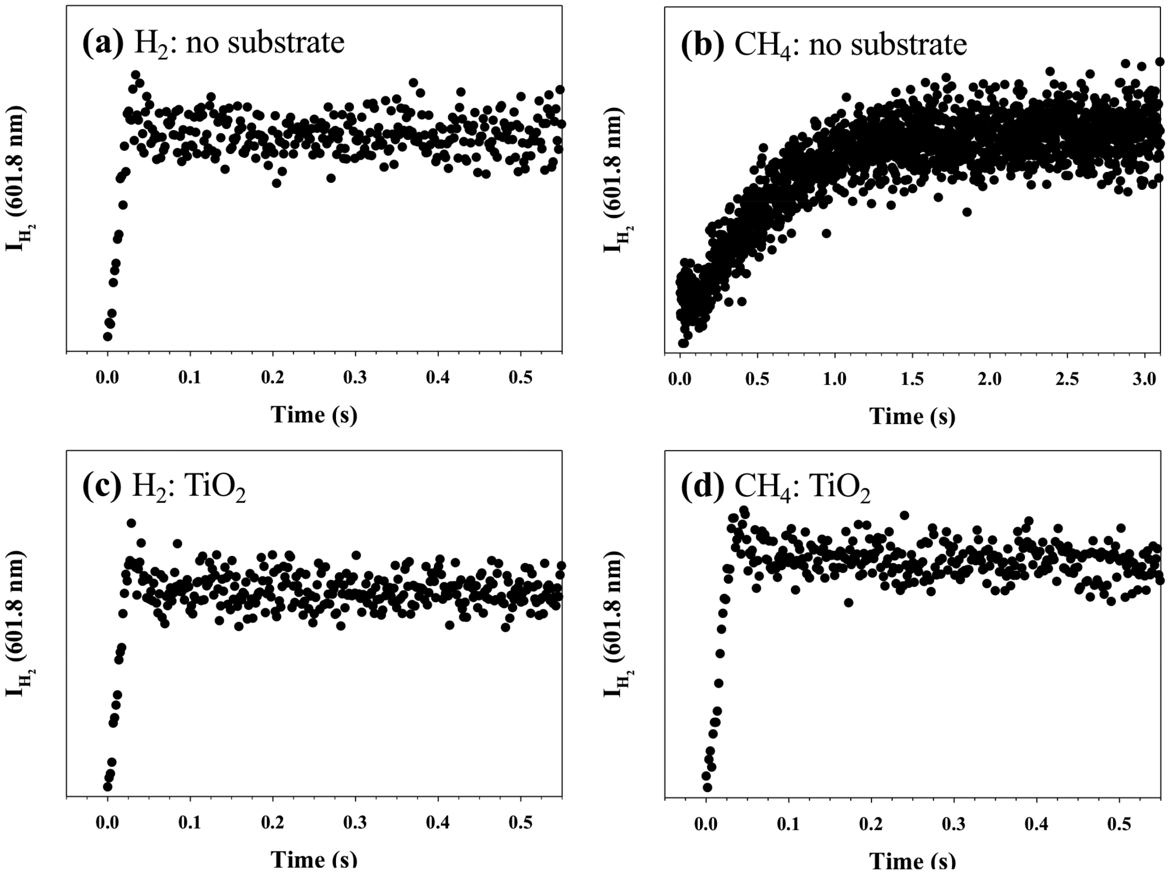

**Figure 10.** Temporal profiles of $H_2$ emission in a $H_2$ plasma (a, c) and a $CH_4$ plasma (b, d) without a substrate (a, b) and with a $TiO_2$ substrate (c, d) at $p$ = 100 mTorr and $P$ = 125 W.

holistic approach toward elucidating the molecular level processes occurring in these inherently complex PAC systems.

A previous study from our lab employed OES to examine the gas phase of $H_2$ plasmas during processing of $SnO_2$ nanomaterials.[28] In that study, excited-state OH and Sn species were observed in the gas phase only when a substrate was placed in the discharge. Similar observations are reported here where raw OES spectra of $H_2$ plasmas show the presence of OH and CO species when a $TiO_2$ substrate is placed in the discharge (Figure 2b). XPS atomic composition data (Table 3) also show a significant reduction of carbon post $H_2$ plasma exposure, suggesting that adventitious carbon is removed from the material surface during plasma processing and is likely the source for the gas-phase CO species. Given that we do not see OH* without a substrate, OH* formation likely occurs through removal of oxygen from the substrate. To elucidate further details about these plasma−surface interactions, we utilized inert gas actinometry to measure relative species densities as functions of plasma parameters (Figure 3), revealing that [H] is not affected by the catalyst when emission is collected coaxially along the length of the reactor. Conversely, [H] in the coil region shows an overall increase compared to the coaxially collected data, presumably resulting from the continuous flow of $H_2$ that can dissociate to H* in the coil. Interestingly, when a $TiO_2$ substrate is placed in the discharge, [H] is significantly reduced only in the coil region of the reactor. Shirazi et al. found that H atoms originating either from dissociative adsorption of $H_2$ or $CH_4$ or from H atoms produced in the bulk plasma can be readily adsorbed on a Ni catalyst.[45] Thus, the significant decrease of [H] directly above the substrate may be a result of adsorption of H atoms on the $TiO_2$ catalyst surface. Conversely, [OH] was similar in both the coil and coaxial data, indicating that once OH* forms in the coil region it persists as it continues downstream in the reactor. One additional noteworthy observation from the Figure 3 actinometry data is that [OH] decreases to nearly zero over the 5 min treatment time. In $H_2$ plasmas, the only source of oxygen is the $TiO_2$ substrate, thereby serving as a limiting reagent for OH species production, especially if surface oxygen were removed from the substrate through plasma processes.

FTIR and XPS results further corroborate the $H_2$ plasma OES data. For example, FTIR data (Figure 5) suggest the creation of a more uniform lattice environment and removal of carbon and oxygen species. Additionally, high-resolution XPS data demonstrate increases in the $-O_{vac}$ and $-O_{surf}$ binding environments (Figures 6b and 6e) and reduction of $Ti^{4+}$ (Figures 6a and 6d) after plasma exposure. Although $Ti^{4+}$ was not always reduced, an increase in the $-O_{vac}$ and $-O_{surf}$ binding environments was always observed post plasma treatment. Changes in atomic composition (Table 3) are noted after 1 and 5 min of plasma exposure ($P$ = 125 W), but atomic compositions are within error for the 5 and 10 min plasma treatments, indicating significant changes to the catalyst's surface chemistry likely occur within the first few minutes of plasma exposure. Together, the OES and materials characterization data suggest etching of surface oxygen by the hydrogen plasma. It is thus useful to consider which gas-phase species act as etchants in this system to further illuminate potential etching mechanisms.

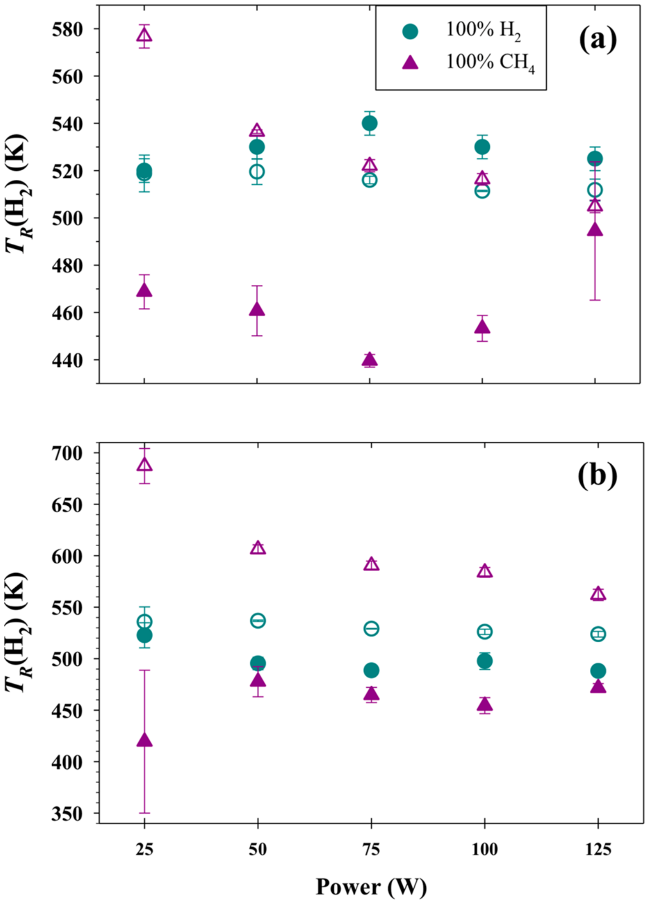

**Figure 11.** $T_R(H_2)$ data as a function of applied rf power for 100% $H_2$ and 100% $CH_4$ plasma systems without (open symbols) and with (closed symbols) a $TiO_2$ substrate at (a) $p$ = 100 mTorr and (b) $p$ = 200 mTorr. Values for $T_R(H_2)$ without a substrate were previously reported in ref 26.

**Table 5. $T_R(H_2)$ (K) Values in 100% $H_2$ and 100% $CH_4$ Plasma Systems**[a]

| | | $H_2$ plasma | | $CH_4$ plasma | |
|---|---|---|---|---|---|
| $p$ (mTorr) | $P$ (W) | no substrate[b] | $TiO_2$ | no substrate[b] | $TiO_2$ |
| 100 | 25 | 520 (10) | 520 (5) | 575 (5) | 470 (10) |
| | 50 | 520 (5) | 530 (5) | 535 (5) | 460 (10) |
| | 75 | 515 (5) | 540 (5) | 520 (5) | 440 (5) |
| | 100 | 510 (5) | 530 (5) | 515 (5) | 455 (10) |
| | 125 | 510 (5) | 525 (5) | 505 (5) | 495 (30) |
| 150 | 25 | 530 (20) | 540 (20) | 605 (10) | 460 (20) |
| | 50 | 525 (5) | 545 (10) | 590 (15) | 450 (10) |
| | 75 | 530 (5) | 550 (15) | 565 (5) | 470 (5) |
| | 100 | 525 (5) | 525 (5) | 560 (5) | 455 (15) |
| | 125 | 525 (5) | 525 (5) | 535 (5) | 450 (10) |
| 200 | 25 | 535 (15) | 520 (15) | 690 (20) | 420 (70) |
| | 50 | 535 (5) | 500 (10) | 605 (5) | 480 (15) |
| | 75 | 530 (5) | 490 (5) | 590 (5) | 465 (10) |
| | 100 | 525 (5) | 500 (10) | 585 (5) | 455 (10) |
| | 125 | 525 (5) | 490 (5) | 560 (5) | 470 (5) |

[a] Values in parentheses represent standard deviation calculated from the mean of $n \geq 3$ trials. [b] "No substrate" values reported previously in ref 26.

Both hydrogen and argon plasma treatments have been used widely as a preparation method for catalyst reduction; consequently, several investigations of the primary etching pathways within these systems have been reported.[46−49] For example, one study suggests the products of electron-mediated reactions with ethanol may be the primary reducing agents in Ar plasmas.[48] Moreover, a recent review of plasma catalyst preparation states that both hydrogen radicals and electrons are strong reducing agents for metal catalysts in $H_2$ plasmas.[49] A previous study from our lab provided a discussion on the potential etchants of $SnO_2$ nanomaterials in low pressure, inductively coupled rf $H_2$/Ar plasmas, concluding that H* acted as the primary etchant.[28] Given the similar parameters utilized in this study, we believe H* acts as the primary etchant here as well. Moreover, the significant decrease in [H] when the catalyst is in the plasma (Figure 3b) indicates that hydrogen atoms interact with the substrate to form OH or other species (e.g., $H_2$).

One approach to discerning key mechanistic processes occurring in our plasma systems includes determination of internal molecular plasma temperatures and trends. For example, $T_R$(OH) and $T_V$(OH) were calculated for the 100% $H_2$ plasma system with $TiO_2$ as OH is an etch product that also changes with plasma parameters. Importantly, a non-Boltzmann distribution behavior is expected for OH $A^2\Sigma^+$, $H_2$ $d^3\Pi_u$, and CH $A^2\Delta$ in low-pressure plasmas because the collisional time frame is on the same order as the radiative lifetimes.[30,50,51] As such, the rotational states have no time to relax before undergoing radiative decay. Thus, $T_R$ values measured in our systems can be used to elucidate formation mechanisms because $T_R$ becomes an image of the formation process rather than the kinetic temperature. Furthermore, some formation mechanisms can favor production of high or low rotational excited states which can drastically change $T_R$ and ultimately provide insight into understanding mechanistic phenomena occurring in our systems.[30]

$T_R$(OH) values cover a fairly large range (~2900−3700 K), and $T_V$(OH) values are routinely higher (~4000−4400 K). Although the representative emission spectrum of the OH $A^2\Sigma^+ \rightarrow X^2\Pi$ transition in Figure 4 shows a high PC value (0.96), our associated experimental error does not allow clear conclusions regarding energy partitioning trends from these data. Nevertheless, we can compare the range of these values to those reported in the literature. Stuckert et al. determined $T_R$(OH) and $T_V$(OH) in $H_2O$ and $H_2$ plasmas with $SnO_2$ nanomaterials under similar pressure and power ranges.[28] Reported $T_V$(OH) values were ~3450−4020 K, and $T_R$(OH) values ranged from ~1800 to 5400 K, with typically higher $T_R$(OH) values reported in the $H_2$ system compared to the $H_2O$ system. Notably, these values generally align with those reported herein. A study by Sarani et al. suggests vibrational−rotational populations of OH can be formed via different mechanisms of generation for excited-state species with different $J$ levels.[29] The authors suggest lower rotational states ($J < 13$) are produced in their system (atmospheric pressure DBD plasma jet, Ar/water vapor mixtures) through a combination of direct electron impact excitation from the ground state and dissociative excitation, resulting in $T_R$(OH) = 625 K. Meanwhile, the $13 < J < 25$ states are characterized by a higher rotational temperature [$T_R$(OH) = 5000 K], suggesting dissociative excitation as the main pathway for OH $A^2\Sigma^+$ formation. Other reported $T_R$(OH $A^2\Sigma^+$) values range from ~450 to 3700 K with $T_V$(OH $A^2\Sigma^+$) = ~6000 K.[30,31] A critical

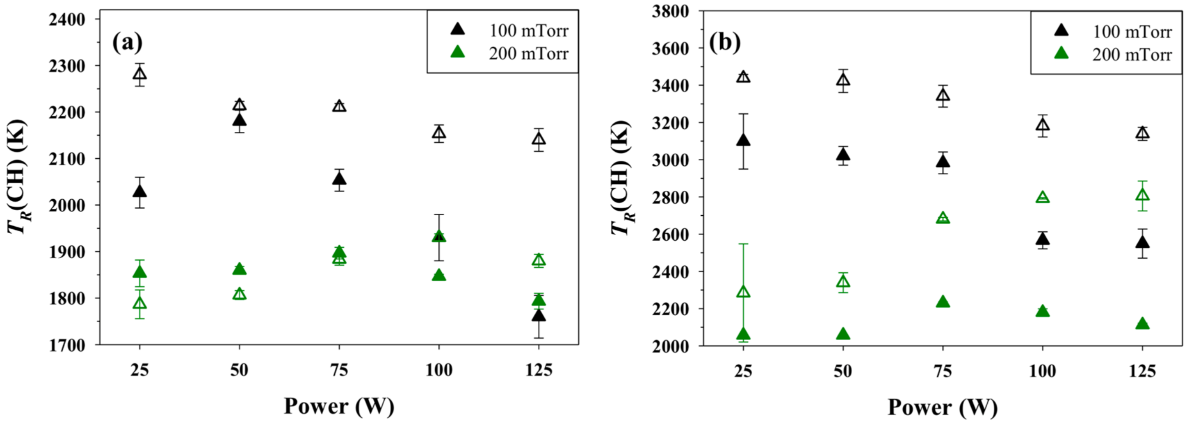

**Figure 12.** (a) $T_R$(CH) and (b) $T_V$(CH) as a function of $P$ for a 100% $CH_4$ plasma without (open triangles) and with a $TiO_2$ substrate (closed triangles). Values for $T_R$(CH) and $T_V$(CH) without substrate were previously reported in ref 25.

**Table 6. $T_R$(CH) and $T_V$(CH) Values in a 100% $CH_4$ Plasma with a $TiO_2$ Substrate**[a]

| | | $T_R$ (K) | | $T_V$ (K) | |
|---|---|---|---|---|---|
| $p$ (mTorr) | $P$ (W) | no substrate[b] | $TiO_2$ | no substrate[b] | $TiO_2$ |
| 100 | 25 | 2280 (20) | 2030 (30) | 3440 (20) | 3100 (150) |
| | 50 | 2210 (10) | 2180 (20) | 3420 (60) | 3020 (50) |
| | 75 | 2210 (10) | 2050 (20) | 3340 (60) | 2980 (60) |
| | 100 | 2150 (20) | 1930 (50) | 3180 (60) | 2570 (50) |
| | 125 | 2240 (20) | 1760 (50) | 3140 (40) | 2550 (80) |
| 150 | 25 | 1910 (20) | 2030 (30) | 2610 (10) | 2680 (70) |
| | 50 | 1960 (10) | 1980 (20) | 2910 (20) | 2480 (50) |
| | 75 | 2070 (10) | 1970 (10) | 3310 (60) | 2620 (40) |
| | 100 | 2010 (10) | 1930 (40) | 3090 (30) | 2690 (30) |
| | 125 | 1980 (40) | 1880 (20) | 3010 (110) | 2680 (120) |
| 200 | 25 | 1790 (30) | 1850 (30) | 2280 (260) | 2060 (10) |
| | 50 | 1810 (10) | 1860 (10) | 2340 (10) | 2060 (10) |
| | 75 | 1880 (10) | 1900 (10) | 2680 (10) | 2230 (10) |
| | 100 | 1930 (10) | 1850 (10) | 2790 (10) | 2180 (20) |
| | 125 | 1880 (10) | 1790 (20) | 2810(80) | 2110 (10) |

[a] Values in parentheses represent standard deviation calculated from the mean of $n \geq 3$ trials. [b] "No substrate" values reported previously in ref 25.

review of $T_R$(OH) determination by Bruggeman and co-workers demonstrates that even at atmospheric pressure, rotational population distributions of OH $A^2\Sigma^+$ provide an image of its formation process.[30] Thus, although many of these literature values arise from atmospheric pressure plasma systems, the wide range of $T_R$(OH) values reported likely evolve from different formation processes.

$T_R$(OH) values are also much larger than $T_R(H_2)$ or $T_R$(CH) values reported herein. In a related study by Cruden et al., rotational temperatures of five molecular species (i.e., CF, CN, CO, $C_2$, and SiF) were measured in a low-pressure (30 mTorr) inductively coupled $CF_4$-based plasma system.[52] The authors determined that SiF, produced solely from plasma−surface interactions with the reactor wall, had a higher rotational temperature (∼2300 K) than those for molecules produced primarily from gas-phase reactions (e.g., CF and CN, ∼1250 K). Species produced via a combination of gas-phase and plasma−surface interactions (identified as CO and $C_2$) exhibited intermediate $T_R$ values of 1600 and 1800 K, respectively. Their results suggest that species produced as etch products leave the surface with significant internal energies and further supports the elevated $T_R$(OH) values measured in our systems.

On the basis of our materials analyses and the measured $T_R$(OH) and $T_V$(OH) values in our plasmas, we determined probable mechanistic pathways for OH* formation, depicted in reactions 1 and 2, where "•" represents an active site on the material surface.

$$H_2^*(g) \rightarrow 2H^*(g) \tag{1}$$

$$H^*(g) + TiO_2(s) \rightarrow OH(g) + \bullet TiO(s) + e^- \tag{2a}$$

$$OH(g) + e^- \rightarrow OH^*(g) + e^- \tag{2b}$$

One reason we included $H_2$ plasmas in our PAC studies is that hydrogen species comprise a significant component of $CH_4$ plasma decomposition. As such, it is important to determine how these species interact with the catalyst. Precursor dissociation in $CH_4$ plasma discharges generally leads to an array of product species such as $CH_x$, H, $H_2$, and $C_2$.[53,54] Consequently, several groups have previously reported on energy partitioning of CH or $C_2$ in $CH_4$ plasmas.[55−58] Electron impact dissociation of $CH_4$ is the dominant pathway for generating these species in the plasma with either subsequent radical recombination reactions to form higher order hydrocarbons or further electron impact dissociation.[9,59] Specifically, reactions 3−5 are hypothesized to be the primary routes for

$CH_4$ decomposition. Simulation of DBD methane plasma conversion showed that reaction 3 accounts for ~79% of electron impact dissociation of $CH_4$ and reactions 4 and 5 account for ~15% and ~5%, respectively.[60]

$$CH_4 + e^- \rightarrow CH_3 + H + e^- \tag{3}$$

$$CH_4 + e^- \rightarrow CH_2 + H_2 + e^- \tag{4}$$

$$CH_4 + e^- \rightarrow CH + H + H_2 + e^- \tag{5}$$

Although formation of CH has been directly related to $CH_4$ decomposition,[58] interpretation of energy partitioning results should also consider the relevant amount of discharge power converted to rotational and vibrational excitation of other species in the plasma. For example, $H_2$ is an important component to $CH_4$ plasma chemistry utilized for production of amorphous hydrocarbon films deposited via PECVD.[53,54,61,62] Furthermore, hydrogen production via hydrocarbon reforming has received much attention as an alternative energy source;[63,64] thus, we sought to combine $T_R(H_2)$ values with energy partitioning trends for CH in $CH_4$ systems.

Our previous study included investigations of $T_R(H_2)$ trends and discussion on probable excitation mechanisms for $H_2$ in 100% $H_2$ and 100% $CH_4$ plasmas sans catalyst.[26] These data are depicted by the open symbols in Figure 11. Notably, $T_R(H_2)$ values (no substrate) are typically higher in 100% $CH_4$ plasmas (~500−700 K) compared to 100% $H_2$ plasmas (~500−550 K). Although discernible differences between $T_R(H_2)$ values and trends in these two plasma systems have been discussed in detail previously,[26] the TR-OES studies performed here lend additional insight into formation mechanisms. Temporal profiles of $H_2$ emission in a 100% $H_2$ plasma and a 100% $CH_4$ plasma without $TiO_2$ (Figures 10a and 10b, respectively) demonstrate clear differences in formation rates. With a $TiO_2$ substrate in the system, little changes for the 100% $H_2$ plasma, whereas a dramatic change in the $H_2$ temporal profile is observed for the $CH_4$ system (Figure 10d). The $H_2$ energetics in these two systems with the catalyst support these TR-OES results. Specifically, in the 100% $H_2$ plasmas, $T_R(H_2)$ values are not significantly altered by the presence of the $TiO_2$ (Figure 11), suggesting $TiO_2$ does not affect $H_2$ excitation pathways in $H_2$ plasmas. Contrarily, $T_R(H_2)$ values in the 100% $CH_4$ plasma decrease by ~100−200 K in the presence of the catalyst, strongly indicating the catalyst plays a significant role in $H_2^*$ formation processes in $CH_4$ plasmas.

Density functional theory (DFT) calculations have recently been used to investigate the interactions of hydrogen species with catalysts and hydrogenation mechanisms in PAC systems.[45,65,66] In one such study, Shirazi et al. examined the diffusion of H atoms to the surface and into the bulk of Ni(111) for different amounts of H atom surface coverage.[45] Their results suggest the H atom coverage on the catalyst can strongly influence reaction kinetics. For example, when a threshold H atom surface coverage is surpassed, adsorption of H atoms or dissociative adsorption of $H_2$ or $CH_4$ becomes an endothermic and, thus, unfavorable process. In this case, associative desorption of $H_2$ or the consumption of surface bound H atoms by another reactant will occur to release active sites for further adsorption of species. A higher rate of H atom diffusion to a subsurface also gives rise to a higher H atom adsorption on the surface, resulting in the reduction of surface bound H atoms, and increases the rate of hydrogenation. Indeed, another study by these authors showed that catalytic hydrogenation reactions proceed faster in the presence of high H coverage.[65] Furthermore, the adsorbate surface coverage is highly dependent on PAC reaction conditions. Thus, changes in plasma parameters can result in significant changes to the surface chemistry and ultimately modify the reaction kinetics at the catalyst surface.

Similar to $T_R(H_2)$ in the 100% $CH_4$ plasma, $T_R(CH)$ also decreases upon the addition of a $TiO_2$ catalyst (Figure 12a, 100 mTorr). Here, $T_R(CH)$ values are reduced by ~100−200 K except at $P = 50$ W, where $T_R(CH)$ values are within error for the no substrate and $TiO_2$ substrate systems. The addition of a substrate to the plasma may impact rotational cooling pathways by providing an extra surface for collisional cooling, leading to the lower $T_R(H_2)$ and $T_R(CH)$ values. Rotational relaxation is a relatively fast process as fewer than ten collisions are typically required to reach equilibrium.[67] Thus, although $T_R(CH)$ decreases with the addition of the catalyst to the discharge at $p = 100$ mTorr, at $p = 150{-}200$ mTorr $T_R(CH)$ values for the catalyst systems are generally within experimental error of the no catalyst system, indicating that gas-phase rotational cooling processes are likely the principal processes occurring at these increased pressures.

Our data clearly demonstrate the impact of a $TiO_2$ catalyst on rotational energy partitioning for $H_2$ $d^3\Pi_u$ and CH $A^2\Delta$ in $CH_4$ plasmas; yet, rotational excitation pathways via electron impact have threshold energies (~0.01−0.1 eV) much lower than activation energies of heterogeneous catalysis reactions.[68] Consequently, the internal energy of rotationally excited species is too low to induce thermal catalysis in plasma. Vibrationally excited species, on the other hand, have threshold energies (~0.1−1 eV) close to or greater than activation energies in catalysis reactions and are typically not de-excited before they reach the catalyst surface (unlike ions and electronically excited species).[68−70] As such, vibrationally excited species can strongly influence plasma−surface interactions in PAC systems. Numerous studies have focused on elevating the vibrational energy of reactants to enhance dissociative adsorption in catalytic reactions. To date, these studies have mainly focused on $CH_4$[71−75] and $N_2$[76−79] because of their applications in $H_2$ generation via methane reforming and $NH_3$ synthesis, respectively. Because dissociative adsorption of $CH_4$ and $N_2$ becomes the rate-limiting steps in catalytic reactions,[68] an understanding of how energy is partitioned into vibrational degrees of freedom and how to ultimately control that energy is key to enhancing conversion rates in PAC systems.

$T_V(CH)$ measured in our plasmas without and with a $TiO_2$ substrate in the discharge indicates $T_V(CH)$ is significantly decreased (~2550−3100 K) upon addition of the catalyst. We have previously illustrated a similar trend in 100% $N_2$ plasmas, where $T_V(N_2)$ was measured without and with two different catalysts: $TiO_2$ and zeolite NaY.[80] In these studies, $T_V(N_2)$ decreased by ~400−1000 K with either catalyst in the discharge. Moreover, when our reactor was lined with multiple catalytic zeolite substrates, the observed decrease in $T_V(N_2)$ was profoundly enhanced. These results suggest that vibrationally excited molecules leave the surface with some energy loss, resulting in the observed reduced $T_V(N_2)$ values.

Notably, an important piece of surface relaxation mechanisms involves the adsorption of the excited species onto the catalyst surface.[1,81] Dombrowski et al. described a precursor-mediated mechanism in which vibrationally excited methane molecules first trap on the catalyst surface via physisorption before chemisorption or desorption occurs.[82] Depending on the vibrational lifetime and nature of the adsorbate/catalyst interaction, the molecule may either desorb with increased vibrational energy from energy exchange with the catalytic surface or the molecule may become vibrationally quenched by the surface interaction. Several studies showed that vibrationally excited methane molecules interact more favorably with catalytic Ni surfaces than ground-state molecules and that ultimately these plasma−catalyst interactions lower the reaction barrier for C−H dissociation of $CH_4$.[23,24,83] One study measured $T_R$ and $T_V$ of CH $A^2\Delta$ in a packed bed DBD reactor filled with $SiO_2$ pellets only and $SiO_2$ with 3 wt % loading of Ni catalyst to elucidate a better understanding of plasma−catalyst synergies in $CH_4$ reforming systems.[23,24] Their OES results show that although $T_R$(CH) remains unchanged by the introduction of the catalyst, the Ni catalyst significantly increases $T_V$(CH) with catalyst bed temperatures but was essentially independent of bed temperature without the catalyst. Specifically, a close examination of the emission spectra for the CH $A^2\Delta \rightarrow X^2\Pi$ band reveals the intensity of the $\nu(0,0)$ and $\nu(1,1)$ vibrational bands are decreased at elevated bed temperatures, whereas the relative intensity of the $\nu(2,2)$ vibrational band is independent of bed temperature. These results suggest that vibrationally excited CH reacts selectively on the catalyst surface, resulting in intensity changes of the $\nu(0,0)$ and $\nu(1,1)$ vibrational bands and, consequently, the observed elevated $T_V$(CH) values.[23] This synergistic effect, however, was only observed when the catalyst bed temperature exceeded 400 °C.

Another study by Tu et al. examined the impact of $TiO_2$ on $T_R(N_2)$ and $T_V(N_2)$ in a $N_2$-packed bed DBD.[84] Similar to the results presented in the Nozaki et al. study of $T_V$(CH),[23] Tu et al. found that $T_V(N_2)$ increased from ∼2300−2800 K to ∼3200−4100 K with the catalyst in the discharge.[84] Upon catalyst packing, the authors also observed a change in the discharge behavior from a filamentary discharge to a combination of surface discharges on the catalyst and micro discharges generated in void spaces between $TiO_2$ pellets. The authors suggest changes in discharge behavior and concomitant increase in $T_V(N_2)$ from catalyst packing coincide with changes in the electron energy distribution function, wherein there is nominally a shift in the distribution to higher energy electrons.

Our results differ from the studies by Nozaki et al.[23] and Tu et al.[84] in that $T_V$ displays the opposite behavior when the catalyst is placed in the discharge (i.e., $T_V$ decreases upon catalyst introduction). Possible explanations for these differences may be related primarily to the differences between the two plasma systems. The DBD systems operate at atmospheric pressure whereas our system operates at much lower pressures. At atmospheric pressure the collisional time is typically shorter than the radiative lifetime of the species of interest.[30] Thus, in our systems fewer collisions are likely to occur compared to the DBD systems. With the addition of a substrate, there is a greater likelihood of productive plasma−surface collisions, effectively quenching the CH excited states.

Furthermore, the catalyst in our system occupies only a small amount of the total volume, whereas the DBD reactors are packed with pellets, allowing more surface area for plasma−catalyst interactions. These interactions can be complex when the catalysts lie within the discharge zone as a variety of species can interact with catalyst. Interactions between the plasma and the catalyst can be viewed from two perspectives: (1) the influence of the catalyst on plasma characteristics and (2) the influence of the plasma on the catalyst. The presence of a catalyst could significantly enhance the electric field, especially around contact points between the pellets/electrodes.[68,85] Several simulation studies have verified that a packed bed reactor could achieve a higher electric field compare with a nonpacked one.[86,87] A higher electric field generally leads to a higher electron energy, which could promote decomposition. Additionally, if the catalyst does indeed enhance the average electron energy, then this enhancement could depend on the amount of catalyst in the discharge. The electron temperature ($T_e$) measured from OES lines in our system (described previously[88]) indicates that $T_e$ ranged from ∼2.4 to 2.7 eV in $CH_4$ plasmas, independent of pressure and power. Moreover, the presence of the $TiO_2$ catalyst does not appreciably affect $T_e$, further suggesting the change in $T_V$(CH) noted in our systems may not arise from a change to the plasma discharge, but rather may be related to vibrational quenching from plasma−surface interactions. Similarly, Nozaki et al. noted that the reduced field and electron density were not affected by the presence of a Ni catalyst in their simulations, indicating that plasma−catalyst reactions were the primary cause for the observed changes in $T_V$(CH).[24]

Herrera et al. further explored synergistic behavior of plasma−catalyst systems in a $N_2/H_2$ packed-bed DBD reactor with three types of transition-metal catalysts on $Al_2O_3$ support (i.e., $Fe/Al_2O_3$, $Ni/Al_2O_3$, and $Co/Al_2O_3$).[89] Their results demonstrate the metal-on-oxide support catalysts had no significant effect on the plasma's electrical or optical properties compared to the same system with just the $Al_2O_3$ support substrate. These results bolster the argument that the observed synergy results from plasma modification of the catalyst surface rather than catalyst modification of the bulk plasma properties. Indeed, plasmas can significantly alter the chemical and morphological properties of catalytic materials in PAC systems; thus, changes to the catalyst properties will, in turn, have an effect on the overall PAC processes.

Our XPS (Table 4 and Figure 7) and Raman data (Figure 8) from catalysts exposed to $CH_4$ plasmas indicate that although amorphous carbon film deposition occurs, the plasma also modifies the underlying substrate under some parameter conditions. High-resolution $Ti_{2p}$ spectra show reduction of Ti from $Ti^{4+}$ to $Ti^{3+}$ at $p$ = 200 mTorr and $P$ = 25 W (Figure 7a), and Raman spectra (Figure 8b) indicate the presence of oxygen vacancies within the material. Indeed, high-resolution $O_{1s}$ data (Figure 7b) show an increase in adsorbed oxygen species after $CH_4$ plasma exposure, also indicative of oxygen vacancies.[35,38] Overall, these results imply concomitant etching and deposition processes occur within the $CH_4$ plasma system. Interestingly, some studies suggest carbon deposition is significantly reduced by synergistic effects during PAC,[68,90] and plasma treatment has been used as a preparation method for catalysts to reduce coke formation.[49,91,92] This plasma treatment step serves to reduce the metal catalyst and results in higher metal dispersion and catalyst reactivity.[90] Plasma treatment for catalyst preparation in PAC systems has been studied primarily with respect to selectivity and conversion efficiencies;[90] thus, fundamental questions regarding the synergistic effects remain unanswered. These ideas could be further explored via a more holistic experimental approach utilizing gas-phase diagnostics and materials analysis to gain additional insight into synergistic plasma−catalyst interactions.

## 5. SUMMARY

As evidenced from our data, the presence of a catalytic material can drastically alter the gas-phase chemistry of the plasma. Within a $CH_4$ plasma, differences in species energetics and kinetics are observed with the introduction of a $TiO_2$ catalyst. Although the catalyst did not affect $T_R(H_2)$ in $H_2$ plasmas, pronounced decreases in $T_R(CH, H_2)$ and $T_V(CH)$ are observed in the $CH_4$ plasmas. TR-OES studies support the $H_2$ energy partitioning results and reveal further details regarding the impact of the catalyst on $H_2$ formation processes. Although disentangling the exact processes from the data presented herein presents numerous challenges, literature DFT studies have demonstrated that surface H atom coverage can strongly influence catalytic hydrogenation processes.[45,65] Because adsorbate surface coverage may be highly dependent on plasma parameters, future investigations should consider these aspects.

Materials characterization reveals an amorphous hydrocarbon film is deposited in the $CH_4$ plasma, although competing etching processes may also be occurring under some conditions. Conversely, materials analysis post $H_2$ plasma exposure reveals that the plasma acts primarily as an etching system. As PAC systems are extremely complex and convoluted, it is difficult to determine whether the catalyst has more influence on the plasma characteristics or the plasma's impact on the catalyst promotes changes. Ultimately, much work remains to be done to deconvolute plasma−catalyst synergies. Although this work emphasized the importance of analyzing both the gas phase and catalyst in PAC systems, additional data on gas−surface interactions are vital to the future of this emerging technology. For example, our imaging of radicals interacting with surfaces (IRIS) technique measures a molecule's propensity to scatter from substrates may provide more evidence for how plasma species interact synergistically with catalysts. Future work should include a holistic experimental approach focused on elucidating interactions at the plasma−surface interface by combining gas-phase diagnostics, IRIS, and comprehensive materials characterization.

## ■ ASSOCIATED CONTENT

### Supporting Information

The Supporting Information is available free of charge at https://pubs.acs.org/doi/10.1021/acs.jpcc.0c10698.

Representative emission spectra for $H_2$ and CH in a $CH_4$ plasma; $H_2$ actinometry data in a $H_2$ plasma (PDF)

## ■ AUTHOR INFORMATION

### Corresponding Author

**Ellen R. Fisher** − *Department of Chemistry, Colorado State University, Fort Collins, Colorado 80524-1872, United States;* orcid.org/0000-0001-6828-8600;
Email: Ellen.Fisher@colostate.edu

### Author

**Tara L. Van Surksum** − *Department of Chemistry, Colorado State University, Fort Collins, Colorado 80524-1872, United States*

Complete contact information is available at:
https://pubs.acs.org/10.1021/acs.jpcc.0c10698

### Notes

The authors declare no competing financial interest.

## ■ ACKNOWLEDGMENTS

This work was supported by funding through Colorado State University, the National Science Foundation (NSF CBET-1803067), and the American Chemical Petroleum Research Fund (ACS PRF 59776-ND6). The authors thank the Justin Sambur research group for support with the Raman spectroscopy analyses and the staff of the CSU Analytical Resources Core for assistance with the XPS and SEM analyses.

## ■ REFERENCES

(1) Neyts, E. C. Plasma-surface interactions in plasma catalysis. *Plasma Chem. Plasma Process.* **2016**, *36* (1), 185−212.

(2) Feng, X.; Liu, H.; He, C.; Shen, Z.; Wang, T. Synergistic effects and mechanism of a non-thermal plasma catalysis system in volatile organic compound removal: a review. *Catal. Sci. Technol.* **2018**, *8* (4), 936−954.

(3) Puliyalil, H.; Jurković, D. L.; Dasireddy, V. D.; Likozar, B. A review of plasma-assisted catalytic conversion of gaseous carbon dioxide and methane into value-added platform chemicals and fuels. *RSC Adv.* **2018**, *8* (48), 27481−27508.

(4) Meyyappan, M. Plasma nanotechnology: past, present and future. *J. Phys. D: Appl. Phys.* **2011**, *44* (17), 174002.

(5) Kim, H.-H.; Ogata, A.; Futamura, S. Oxygen partial pressure-dependent behavior of various catalysts for the total oxidation of VOCs using cycled system of adsorption and oxygen plasma. *Appl. Catal., B* **2008**, *79* (4), 356−367.

(6) Mustafa, M. F.; Fu, X.; Liu, Y.; Abbas, Y.; Wang, H.; Lu, W. Volatile organic compounds (VOCs) removal in non-thermal plasma double dielectric barrier discharge reactor. *J. Hazard. Mater.* **2018**, *347*, 317−324.

(7) Pan, K. L.; Chang, M. B. Plasma catalytic oxidation of toluene over double perovskite-type oxide via packed-bed DBD. *Environ. Sci. Pollut. Res.* **2019**, *26* (13), 12948−12962.

(8) Shang, S.; Liu, G.; Chai, X.; Tao, X.; Li, X.; Bai, M.; Chu, W.; Dai, X.; Zhao, Y.; Yin, Y. Research on Ni/$\gamma$-$Al_2O_3$ catalyst for $CO_2$ reforming of $CH_4$ prepared by atmospheric pressure glow discharge plasma jet. *Catal. Today* **2009**, *148* (3−4), 268−274.

(9) Tu, X.; Whitehead, J. Plasma-catalytic dry reforming of methane in an atmospheric dielectric barrier discharge: Understanding the synergistic effect at low temperature. *Appl. Catal., B* **2012**, *125*, 439−448.

(10) Li, D.; Rohani, V.; Fabry, F.; Ramaswamy, A. P.; Sennour, M.; Fulcheri, L. Direct conversion of $CO_2$ and $CH_4$ into liquid chemicals by plasma-catalysis. *Appl. Catal., B* **2020**, *261*, 118228.

(11) Arbag, H.; Yasyerli, S.; Yasyerli, N.; Dogu, G.; Dogu, T. Enhancement of catalytic performance of Ni based mesoporous alumina by Co incorporation in conversion of biogas to synthesis gas. *Appl. Catal., B* **2016**, *198*, 254−265.

(12) Angeli, S. D.; Turchetti, L.; Monteleone, G.; Lemonidou, A. A. Catalyst development for steam reforming of methane and model biogas at low temperature. *Appl. Catal., B* **2016**, *181*, 34−46.

(13) Fedorova, Z.; Danilova, M.; Zaikovskii, V. Porous nickel-based catalysts for tri-reforming of methane to synthesis gas: catalytic activity. *Mater. Lett.* **2020**, *261*, 127087.

(14) Lašič Jurković, D.; Puliyalil, H.; Pohar, A.; Likozar, B. Plasma-activated methane partial oxidation reaction to oxygenate platform chemicals over Fe, Mo, Pd and zeolite catalysts. *Int. J. Energy Res.* **2019**, *43* (14), 8085−8099.

(15) Zeng, Y.; Wang, L.; Wu, C.; Wang, J.; Shen, B.; Tu, X. Low temperature reforming of biogas over K-, Mg- and Ce-promoted Ni/$Al_2O_3$ catalysts for the production of hydrogen rich syngas: understanding the plasma-catalytic synergy. *Appl. Catal., B* **2018**, *224*, 469−478.

(16) Bogaerts, A.; Tu, X.; Whitehead, J. C.; Centi, G.; Lefferts, L.; Guaitella, O.; Azzolina-Jury, F.; Kim, H.-H.; Murphy, A. B.;

Schneider, W. F.; et al. The 2020 plasma catalysis roadmap. *J. Phys. D: Appl. Phys.* **2020**, *53* (44), 443001.

(17) Brune, L.; Ozkan, A.; Genty, E.; de Bocarmé, T. V.; Reniers, F. Dry reforming of methane via plasma-catalysis: influence of the catalyst nature supported on alumina in a packed-bed DBD configuration. *J. Phys. D: Appl. Phys.* **2018**, *51* (23), 234002.

(18) Chawdhury, P.; Wang, Y.; Ray, D.; Mathieu, S.; Wang, N.; Harding, J.; Bin, F.; Tu, X.; Subrahmanyam, C. A promising plasma-catalytic approach towards single-step methane conversion to oxygenates at room temperature. *Appl. Catal., B* **2021**, *284*, 119735.

(19) Malik, M. A.; Minamitani, Y.; Schoenbach, K. H. Comparison of catalytic activity of aluminum oxide and silica gel for decomposition of volatile organic compounds (VOCs) in a plasmacatalytic reactor. *IEEE Trans. Plasma Sci.* **2005**, *33* (1), 50−56.

(20) Mizuno, A. Generation of non-thermal plasma combined with catalysts and their application in environmental technology. *Catal. Today* **2013**, *211*, 2−8.

(21) Van Durme, J.; Dewulf, J.; Sysmans, W.; Leys, C.; Van Langenhove, H. Abatement and degradation pathways of toluene in indoor air by positive corona discharge. *Chemosphere* **2007**, *68* (10), 1821−1829.

(22) Nozaki, T.; Agıral, A.ıl; Yuzawa, S.; Han Gardeniers, J. G. E.; Okazaki, K. A single step methane conversion into synthetic fuels using microplasma reactor. *Chem. Eng. J.* **2011**, *166* (1), 288−293.

(23) Nozaki, T.; Muto, N.; Kadio, S.; Okazaki, K. Dissociation of vibrationally excited methane on Ni catalyst: part 2. Process diagnostics by emission spectroscopy. *Catal. Today* **2004**, *89* (1−2), 67−74.

(24) Nozaki, T.; Muto, N.; Kado, S.; Okazaki, K. Dissociation of vibrationally excited methane on Ni catalyst: Part 1. Application to methane steam reforming. *Catal. Today* **2004**, *89* (1−2), 57−65.

(25) Van Surksum, T. L.; Blechle, J. M.; Fisher, E. R. Determination of rotational and vibrational temperatures of CH in $CH_4$ plasmas. *J. Vac. Sci. Technol., A* **2018**, *36* (4), 041302.

(26) Van Surksum, T. L.; Fisher, E. R. Gas-phase diagnostic studies of $H_2$ and $CH_4$ inductively coupled plasmas. *J. Vac. Sci. Technol., A* **2020**, *38* (3), 033010.

(27) Luque, J.; Crosley, D. R. LIFBASE: Database and spectral simulation program (version 1.5). *SRI International Report MP* **1999**, *99* (009).

(28) Stuckert, E. P.; Miller, C. J.; Fisher, E. R. Gas-phase diagnostics during $H_2$ and $H_2O$ plasma treatment of $SnO_2$ nanomaterials: implications for surface modification. *J. Vac. Sci. Technol., B: Nanotechnol. Microelectron.: Mater., Process., Meas., Phenom.* **2017**, *35* (2), 021802.

(29) Sarani, A.; Nikiforov, A. Y.; Leys, C. Atmospheric pressure plasma jet in Ar and Ar/$H_2O$ mixtures: optical emission spectroscopy and temperature measurements. *Phys. Plasmas* **2010**, *17* (6), 063504.

(30) Bruggeman, P.; Schram, D. C.; Kong, M. G.; Leys, C. Is the rotational temperature of OH (A−X) for discharges in and in contact with liquids a good diagnostic for determining the gas temperature? *Plasma Processes Polym.* **2009**, *6* (11), 751−762.

(31) Mukasa, S.; Nomura, S.; Toyota, H.; Maehara, T.; Abe, F.; Kawashima, A. Temperature distributions of radio-frequency plasma in water by spectroscopic analysis. *J. Appl. Phys.* **2009**, *106* (11), 113302.

(32) Bezrodna, T.; Puchkovska, G.; Shymanovska, V.; Baran, J.; Ratajczak, H. IR-analysis of H-bonded $H_2O$ on the pure $TiO_2$ surface. *J. Mol. Struct.* **2004**, *700* (1−3), 175−181.

(33) León, A.; Reuquen, P.; Garín, C.; Segura, R.; Vargas, P.; Zapata, P.; Orihuela, P. A. FTIR and Raman characterization of $TiO_2$ nanoparticles coated with polyethylene glycol as carrier for 2-methoxyestradiol. *Appl. Sci.* **2017**, *7* (1), 49.

(34) Stuckert, E. P.; Fisher, E. R. Ar/$O_2$ and $H_2O$ plasma surface modification of $SnO_2$ nanomaterials to increase surface oxidation. *Sens. Actuators, B* **2015**, *208*, 379−388.

(35) Wu, H.; Xu, C.; Xu, J.; Lu, L.; Fan, Z.; Chen, X.; Song, Y.; Li, D. Enhanced supercapacitance in anodic $TiO_2$ nanotube films by hydrogen plasma treatment. *Nanotechnology* **2013**, *24* (45), 455401.

(36) Ahn, K.; Lee, H.-U.; Jeong, S.-Y.; Kim, J.-P.; Jin, J. S.; Ahn, H.-S.; Kim, H.-S.; Cho, C.-R. Plasma treatment effect on dye-sensitized solar cell efficiency of hydrothermal-processed $TiO_2$ nanorods. *J. Nanosci. Nanotechnol.* **2012**, *12* (7), 6022−6025.

(37) Achour, A.; Islam, M.; Solaymani, S.; Vizireanu, S.; Saeed, K.; Dinescu, G. Influence of plasma functionalization treatment and gold nanoparticles on surface chemistry and wettability of reactive-sputtered $TiO_2$ thin films. *Appl. Surf. Sci.* **2018**, *458*, 678−685.

(38) Han, J.-B.; Wang, X.; Wang, N.; Wei, Z.-H.; Yu, G.-P.; Zhou, Z.-G.; Wang, Q.-Q. Effect of plasma treatment on hydrophilic properties of $TiO_2$ thin films. *Surf. Coat. Technol.* **2006**, *200* (16−17), 4876−4878.

(39) Jensen, H.; Soloviev, A.; Li, Z.; Søgaard, E. G. XPS and FTIR investigation of the surface properties of different prepared titania nano-powders. *Appl. Surf. Sci.* **2005**, *246* (1−3), 239−249.

(40) Kundu, S.; Wang, Y.; Xia, W.; Muhler, M. Thermal stability and reducibility of oxygen-containing functional groups on multiwalled carbon nanotube surfaces: a quantitative high-resolution XPS and TPD/TPR study. *J. Phys. Chem. C* **2008**, *112* (43), 16869−16878.

(41) Choudhury, B.; Choudhury, A. Dopant induced changes in structural and optical properties of $Cr^{3+}$ doped $TiO_2$ nanoparticles. *Mater. Chem. Phys.* **2012**, *132* (2−3), 1112−1118.

(42) Chen, G.; Britun, N.; Godfroid, T.; Georgieva, V.; Snyders, R.; Delplancke-Ogletree, M. Efficient $CO_2$ conversion in microwave plasma via plasma catalysis. *J. Phys. D: Appl. Phys.* **2017**, *50*, 084001.

(43) Tian, F.; Zhang, Y.; Zhang, J.; Pan, C. Raman spectroscopy: a new approach to measure the percentage of anatase $TiO_2$ exposed (001) facets. *J. Phys. Chem. C* **2012**, *116* (13), 7515−7519.

(44) Sarkar, A.; Khan, G. G. The formation and detection techniques of oxygen vacancies in titanium oxide-based nanostructures. *Nanoscale* **2019**, *11* (8), 3414−3444.

(45) Shirazi, M.; Bogaerts, A.; Neyts, E. C. A DFT study of H-dissolution into the bulk of a crystalline Ni (111) surface: a chemical identifier for the reaction kinetics. *Phys. Chem. Chem. Phys.* **2017**, *19* (29), 19150−19158.

(46) Zhang, Y.; Chu, W.; Cao, W.; Luo, C.; Wen, X.; Zhou, K. A plasma-activated Ni/$\alpha$-$Al_2O_3$ catalyst for the conversion of $CH_4$ to syngas. *Plasma Chem. Plasma Process.* **2000**, *20* (1), 137−144.

(47) Ihara, T.; Miyoshi, M.; Ando, M.; Sugihara, S.; Iriyama, Y. Preparation of a visible-light-active $TiO_2$ photocatalyst by RF plasma treatment. *J. Mater. Sci.* **2001**, *36* (17), 4201−4207.

(48) Di, L.; Li, Z.; Lee, B.; Park, D.-W. An alternative atmospheric-pressure cold plasma method for synthesizing Pd/P25 catalysts with the assistance of ethanol. *Int. J. Hydrogen Energy* **2017**, *42* (16), 11372−11378.

(49) Wang, Z.; Zhang, Y.; Neyts, E. C.; Cao, X.; Zhang, X.; Jang, B. W.-L.; Liu, C.-j. Catalyst preparation with plasmas: how does it work? *ACS Catal.* **2018**, *8* (3), 2093−2110.

(50) Vankan, P.; Schram, D.; Engeln, R. Atomic and molecular hydrogen densities in a plasma expansion. *Plasma Sources Sci. Technol.* **2005**, *14* (4), 744.

(51) Luque, J.; Kraus, M.; Wokaun, A.; Haffner, K.; Kogelschatz, U.; Eliasson, B. Gas temperature measurement in $CH_4$/$CO_2$ dielectric-barrier discharges by optical emission spectroscopy. *J. Appl. Phys.* **2003**, *93* (8), 4432−4438.

(52) Cruden, B. A.; Rao, M.; Sharma, S. P.; Meyyappan. Neutral gas temperature estimates in an inductively coupled $CF_4$ plasma by fitting diatomic emission spectra. *J. Appl. Phys.* **2002**, *91* (11), 8955−8964.

(53) Truscott, B. S.; Kelly, M. W.; Potter, K. J.; Ashfold, M. N.; Mankelevich, Y. A. Microwave plasma-activated chemical vapor deposition of nitrogen-doped diamond. II: $CH_4$/$N_2$/$H_2$ plasmas. *J. Phys. Chem. A* **2016**, *120* (43), 8537−8549.

(54) Li, H.; Yang, K.; Liu, H.; Zhu, X. Optical and mass spectroscopic properties of microwave $CH_4$/$H_2$/Ar plasma for diamond deposition in a resonance cavity. *Vacuum* **2018**, *147*, 45−50.

(55) Zhang, S.; Gao, Y.; Sun, H.; Bai, H.; Wang, R.; Shao, T. Time-resolved characteristics and chemical kinetics of non-oxidative methane conversion in repetitively pulsed dielectric barrier discharge plasmas. *J. Phys. D: Appl. Phys.* **2018**, *51* (27), 274005.

(56) Wang, X.; Gao, Y.; Zhang, S.; Sun, H.; Li, J.; Shao, T. Nanosecond pulsed plasma assisted dry reforming of $CH_4$: The effect of plasma operating parameters. *Appl. Energy* **2019**, *243*, 132−144.

(57) Duten, X.; Rousseau, A.; Gicquel, A.; Leprince, P. Rotational temperature measurements of excited and ground states of $C_2$ ($d^3\Pi_g$−$a^3\Pi_u$) transition in a $H_2/CH_4$ 915 MHz microwave pulsed plasma. *J. Appl. Phys.* **1999**, *86* (9), 5299−5301.

(58) Heintze, M.; Magureanu, M.; Kettlitz, M. Mechanism of $C_2$ hydrocarbon formation from methane in a pulsed microwave plasma. *J. Appl. Phys.* **2002**, *92* (12), 7022−7031.

(59) Nair, S.; Nozaki, T.; Okazaki, K. Methane oxidative conversion pathways in a dielectric barrier discharge reactor—investigation of gas phase mechanism. *Chem. Eng. J.* **2007**, *132* (1−3), 85−95.

(60) De Bie, C.; Verheyde, B.; Martens, T.; van Dijk, J.; Paulussen, S.; Bogaerts, A. Fluid modeling of the conversion of methane into higher hydrocarbons in an atmospheric pressure dielectric barrier discharge. *Plasma Processes Polym.* **2011**, *8* (11), 1033−1058.

(61) Ito, H.; Koshimura, K.; Onitsuka, S.; Okada, K.; Suzuki, T.; Akasaka, H.; Saitoh, H. Dissociative Excitation of $C_2H_2$ in the Electron Cyclotron Resonance Plasma of Ar: Production of CH ($A^2\Delta$) Radicals and Formation of Hydrogenated Amorphous Carbon Films. *Plasma Chem. Plasma Process.* **2012**, *32* (2), 231−248.

(62) Pothiraja, R.; Engelhardt, M.; Bibinov, N.; Awakowicz, P. Film deposition on the inner surface of tubes using atmospheric-pressure Ar−$CH_4$, Ar−$C_2H_2$ and Ar−$C_2H_2$−$H_2$ plasmas: interpretation of film properties from plasma-chemical kinetics. *J. Phys. D: Appl. Phys.* **2012**, *45* (33), 335202.

(63) Chung, W.-C.; Chang, M.-B. Review of catalysis and plasma performance on dry reforming of $CH_4$ and possible synergistic effects. *Renewable Sustainable Energy Rev.* **2016**, *62*, 13−31.

(64) Gao, Y.; Jiang, J.; Meng, Y.; Yan, F.; Aihemaiti, A. A review of recent developments in hydrogen production via biogas dry reforming. *Energy Convers. Manage.* **2018**, *171*, 133−155.

(65) Shirazi, M.; Neyts, E. C.; Bogaerts, A. DFT study of Ni-catalyzed plasma dry reforming of methane. *Appl. Catal., B* **2017**, *205*, 605−614.

(66) Somers, W.; Bogaerts, A.; Van Duin, A.; Neyts, E. Plasma species interacting with nickel surfaces: toward an atomic scale understanding of plasma-catalysis. *J. Phys. Chem. C* **2012**, *116* (39), 20958−20965.

(67) Brown, M. S.; Forlines, R. A.; Ganguly, B. N. Measurement of CH density in a pulsed-dc hydrocarbon-gas-mixture discharge. *J. Appl. Phys.* **2005**, *97* (10), 103302.

(68) Chen, H. L.; Lee, H. M.; Chen, S. H.; Chao, Y.; Chang, M. B. Review of plasma catalysis on hydrocarbon reforming for hydrogen production—interaction, integration, and prospects. *Appl. Catal., B* **2008**, *85* (1−2), 1−9.

(69) Gicquel, A.; Cavadias, S.; Amouroux, J. Heterogeneous catalysis in low-pressure plasmas. *J. Phys. D: Appl. Phys.* **1986**, *19* (11), 2013.

(70) Rapakoulias, D.; Cavadias, S.; Mataras, D. Heterogeneous catalysis in interaction of plasma excited species with surfaces. *High Temp. Chem. Process.* **1993**, *2*, 231−246.

(71) Holmblad, P. M.; Wambach, J.; Chorkendorff, I. Molecular beam study of dissociative sticking of methane on Ni (100). *J. Chem. Phys.* **1995**, *102* (20), 8255−8263.

(72) Walker, A.; King, D. Dynamics of dissociative methane adsorption on metals: $CH_4$ on Pt {110}(1× 2). *J. Chem. Phys.* **2000**, *112* (10), 4739−4748.

(73) Higgins, J.; Conjusteau, A.; Scoles, G.; Bernasek, S. State selective vibrational ($2\nu_3$) activation of the chemisorption of methane on Pt (111). *J. Chem. Phys.* **2001**, *114* (12), 5277−5283.

(74) Beck, R. D.; Maroni, P.; Papageorgopoulos, D. C.; Dang, T. T.; Schmid, M. P.; Rizzo, T. R. Vibrational mode-specific reaction of methane on a nickel surface. *Science* **2003**, *302* (5642), 98−100.

(75) Jackson, B.; Nave, S. The dissociative chemisorption of methane on Ni (111): The effects of molecular vibration and lattice motion. *J. Chem. Phys.* **2013**, *138* (17), 174705.

(76) Rettner, C.; Stein, H. Effect of vibrational energy on the dissociative chemisorption of $N_2$ on Fe (111). *J. Chem. Phys.* **1987**, *87* (1), 770−771.

(77) Romm, L.; Katz, G.; Kosloff, R.; Asscher, M. Dissociative chemisorption of $N_2$ on Ru (001) enhanced by vibrational and kinetic energy: Molecular beam experiments and quantum mechanical calculations. *J. Phys. Chem. B* **1997**, *101* (12), 2213−2217.

(78) Mehta, P.; Barboun, P.; Herrera, F. A.; Kim, J.; Rumbach, P.; Go, D. B.; Hicks, J. C.; Schneider, W. F. Overcoming ammonia synthesis scaling relations with plasma-enabled catalysis. *Nat. Catal.* **2018**, *1* (4), 269−275.

(79) Rouwenhorst, K. H.; Kim, H.-H.; Lefferts, L. Vibrationally excited activation of $N_2$ in plasma-enhanced catalytic ammonia synthesis: a kinetic analysis. *ACS Sustainable Chem. Eng.* **2019**, *7* (20), 17515−17522.

(80) Hanna, A. R.; Van Surksum, T. L.; Fisher, E. R. Investigating the impact of catalysts on $N_2$ rotational and vibrational temperatures in low pressure plasmas. *J. Phys. D: Appl. Phys.* **2019**, *52* (34), 345202.

(81) Whitehead, J. C. Plasma−catalysis: the known knowns, the known unknowns and the unknown unknowns. *J. Phys. D: Appl. Phys.* **2016**, *49* (24), 243001.

(82) Dombrowski, E.; Peterson, E.; Del Sesto, D.; Utz, A. Precursor-mediated reactivity of vibrationally hot molecules: Methane activation on Ir (1 1 1). *Catal. Today* **2015**, *244*, 10−18.

(83) Kim, J.; Abbott, M. S.; Go, D. B.; Hicks, J. C. Enhancing C−H bond activation of methane via temperature-controlled, catalyst−plasma interactions. *ACS Energy Lett.* **2016**, *1* (1), 94−99.

(84) Tu, X.; Gallon, H. J.; Whitehead, J. C. Electrical and spectroscopic diagnostics of a single-stage plasma-catalysis system: effect of packing with $TiO_2$. *J. Phys. D: Appl. Phys.* **2011**, *44* (48), 482003.

(85) Neyts, E. C.; Ostrikov, K.; Sunkara, M. K.; Bogaerts, A. Plasma catalysis: synergistic effects at the nanoscale. *Chem. Rev.* **2015**, *115* (24), 13408−13446.

(86) Van Laer, K.; Bogaerts, A. Fluid modelling of a packed bed dielectric barrier discharge plasma reactor. *Plasma Sources Sci. Technol.* **2016**, *25* (1), 015002.

(87) Kruszelnicki, J.; Engeling, K. W.; Foster, J. E.; Xiong, Z.; Kushner, M. J. Propagation of negative electrical discharges through 2-dimensional packed bed reactors. *J. Phys. D: Appl. Phys.* **2017**, *50* (2), 025203.

(88) Hanna, A. R.; Blechle, J. M.; Fisher, E. R. Using Fundamental Spectroscopy to Elucidate Kinetic and Energetic Mechanisms within Environmentally Relevant Inductively Coupled Plasma Systems. *J. Phys. Chem. A* **2017**, *121* (40), 7627−7640.

(89) Herrera, F. A.; Brown, G. H.; Barboun, P.; Turan, N.; Mehta, P.; Schneider, W. F.; Hicks, J. C.; Go, D. B. The impact of transition metal catalysts on macroscopic dielectric barrier discharge (DBD) characteristics in an ammonia synthesis plasma catalysis reactor. *J. Phys. D: Appl. Phys.* **2019**, *52* (22), 224002.

(90) Chen, H. L.; Lee, H. M.; Chen, S. H.; Chang, M. B.; Yu, S. J.; Li, S. N. Removal of volatile organic compounds by single-stage and two-stage plasma catalysis systems: a review of the performance enhancement mechanisms, current status, and suitable applications. *Environ. Sci. Technol.* **2009**, *43* (7), 2216−2227.

(91) Yan, X.; Zhao, B.; Liu, Y.; Li, Y. Dielectric barrier discharge plasma for preparation of Ni-based catalysts with enhanced coke resistance: current status and perspective. *Catal. Today* **2015**, *256*, 29−40.

(92) Chen, G.; Britun, N.; Godfroid, T.; Georgieva, V.; Snyders, R.; Delplancke-Ogletree, M.-P. An overview of $CO_2$ conversion in a microwave discharge: the role of plasma-catalysis. *J. Phys. D: Appl. Phys.* **2017**, *50* (8), 084001.